

A Numerical Study of the June 2013 Flood-Producing Extreme Rainstorm over Southern Alberta

YANPING LI,^a KIT SZETO,^b RONALD E. STEWART,^c JULIE M. THÉRIAULT,^d LIANG CHEN,^{a,e}
BOHDAN KOCHTUBAJDA,^f ANTHONY LIU,^f SUDESH BOODOO,^g RON GOODSON,^f
CURTIS MOONEY,^f AND SOPAN KURKUTE^a

^a *Global Institute for Water Security, University of Saskatchewan, Saskatoon, Saskatchewan, Canada*

^b *Environment and Climate Change Canada, Toronto, Ontario, Canada*

^c *Department of Environment and Geography, University of Manitoba, Winnipeg, Manitoba, Canada*

^d *Department of Earth and Atmospheric Sciences, Université du Québec à Montréal, Montreal, Quebec, Canada*

^e *Key Laboratory of Regional Climate Environment for Temperate East Asia, Institute of Atmospheric Physics, Chinese Academy of Sciences, Beijing, China*

^f *Environment and Climate Change Canada, Edmonton, Alberta, Canada*

^g *Environment and Climate Change Canada, King City, Ontario, Canada*

(Manuscript received 24 September 2015, in final form 16 April 2017)

ABSTRACT

A devastating, flood-producing rainstorm occurred over southern Alberta, Canada, from 19 to 22 June 2013. The long-lived, heavy rainfall event was a result of complex interplays between topographic, synoptic, and convective processes that rendered an accurate simulation of this event a challenging task. In this study, the Weather Research and Forecasting (WRF) Model was used to simulate this event and was validated against several observation datasets. Both the timing and location of the model precipitation agree closely with the observations, indicating that the WRF Model is capable of reproducing this type of severe event. Sensitivity tests with different microphysics schemes were conducted and evaluated using equitable threat and bias frequency scores. The WRF double-moment 6-class microphysics scheme (WDM6) generally performed better when compared with other schemes. The application of a conventional convective/stratiform separation algorithm shows that convective activity was dominant during the early stages, then evolved into predominantly stratiform precipitation later in the event. The HYSPLIT back-trajectory analysis and regional water budget assessments using WRF simulation output suggest that the moisture for the precipitation was mainly from recycling antecedent soil moisture through evaporation and evapotranspiration over the Canadian Prairies and the U.S. Great Plains. This analysis also shows that a small fraction of the moisture can be traced back to the northeastern Pacific, and direct uptake from the Gulf of Mexico was not a significant source in this event.

1. Introduction

There is increasing evidence that global climate change has affected the occurrence of extreme weather events in many parts of the world (IPCC 2012; Zhang et al. 2000). In particular, flooding has become more frequent during the last few decades in many regions (IPCC 2012, chapter 3), especially downwind of significant terrain in the mid-latitudes of continents (Colle et al. 2013; Garreaud and Fuenzalida 2007; Rasmussen et al. 2015; Szeto et al. 2015). The Canadian Prairies are located east of the Canadian Rockies and account for 80% of Canada's irrigated and rain-fed agriculture (Wheater and Gober 2013).

This region is subjected to extreme precipitation and flooding events. Floods in April and May are mainly associated with runoff, ice-jam breaks, or rain-on-snow events, while flooding from June to September is frequently associated with heavy precipitation generated by convective and synoptic weather systems. This growing season rainfall is also critical to the region's hydrology and water management (Zhang et al. 2001; Szeto et al. 2011; Shook and Pomeroy 2012; McDonald and Dyck 2006).

During 19–22 June 2013, a catastrophic flooding event occurred over southern Alberta. The flood was caused by heavy rainfall and additional runoff from snowmelt, which occurred after a prolonged period of unusually wet conditions (Pomeroy et al. 2015). Many regions of southwestern Alberta, including the city of Calgary, were

Corresponding author: Yanping Li, yanping.li@usask.ca

DOI: 10.1175/JHM-D-15-0176.1

© 2017 American Meteorological Society. For information regarding reuse of this content and general copyright information, consult the [AMS Copyright Policy](http://www.ametsoc.org/PUBSReuseLicenses) (www.ametsoc.org/PUBSReuseLicenses).

significantly affected, with five deaths and total economic losses in excess of CAD \$6 billion (Milrad et al. 2015).

Extreme rainstorms over southern Alberta have been examined in previous studies and several common features were noted. These storms are typically associated with a deep shortwave trough or an upper-cutoff, low pressure system over the west coast of North America, with a surface low pressure system developing east of the Rockies near the Canada–U.S. border, and enhanced transport of water vapor toward the foothills by low-level synoptic-scale flow features (Szeto et al. 2011). The complex interactions between atmospheric and hydrological processes such as snowmelt and rain on snow, as well as the proximity of the Rocky Mountains, can produce heavy rainfall in the foothills and front ranges, which have triggered most of the major floods in the region (Szeto et al. 2011; Flesch and Reuter 2012; Pennelly et al. 2014). A recent numerical simulation suggests that the Rockies influence precipitation amounts and duration in the mountains and foothills due to orographic lifting (Flesch and Reuter 2012).

Similar features were observed in flood-producing rainstorms east of the Rockies in the United States (Maddox et al. 1980, 1978; Caracena et al. 1979; Gochis et al. 2015). Quasi-stationary synoptic patterns, high precipitation efficiency, effective lifting mechanisms, moisture-rich flow, and longevity of the rainfall were significant contributors to these flash flooding events. The spatial structure and temporal evolution of flood-producing rainfall associated with mesoscale convective systems (MCSs) in the area east of the Rocky Mountains were summarized by Schumacher and Johnson (2005). East of the Rockies, eastward-propagating precipitating systems with embedded MCSs were organized by mid- or low-level jets, and the associated floods were likely a result of deep moisture advection toward the mountains throughout the troposphere, as well as through interactions with the terrain, such as, the Big Thompson 1976 and Rapid City 1972 flash floods (Maddox et al. 1980, 1978; Caracena et al. 1979) and the September 2013 Colorado flood (Gochis et al. 2015). With similar terrain arrangement as the 2013 Alberta event, a cutoff low with preconditioning of the land surface also occurred on the lee side of the Rockies during the Colorado flood of September 2013 (Gochis et al. 2015).

A recent flood in Leh, India also showed similarities to the Big Thompson 1976, Rapid City 1972, and Colorado 2013 flash floods, especially with respect to processes and orographic characteristics. However, the Leh flood was the result of a series of westward-propagating MCSs forming upstream over the Tibetan Plateau, whereas the Big Thompson flood resulted from continuously regenerating nonpropagating storms that remained

downslope of the steep terrain (Rasmussen and Houze 2012). Previous studies also suggested that both local and remote sources of moisture could be important in producing intense rainfall and floods over various regions of the continent (e.g., Turato et al. 2004; Brimelow and Reuter 2005; Stohl and James 2004).

In this study, the Weather Research and Forecasting (WRF) Model (Skamarock et al. 2008) is used to simulate the major rainstorm that played a critical role in producing the 2013 southern Alberta flood (hereafter referred to as the J13 storm). Several sensitivity experiments with different microphysical schemes were carried out in order to assess the WRF Model's ability to simulate the storm. Simulation results are evaluated using equitable threat and bias frequency scores. A conventional convective/stratiform separation algorithm is applied to examine the evolution of storm characteristics during the life cycle of the flood event. Regional water budget assessments and air parcel back-trajectory analyses are carried out to examine the sources and transport of the remote moisture for the J13 storm. This article is a follow-up to two companion papers that discuss the synoptic and observational aspects of the J13 storm (Liu et al. 2016; Kochtubajda et al. 2016).

The goal of this study is to improve understanding and prediction of flash floods occurring on the plains downwind of significant terrain and to contribute to the understanding of the interaction between orographic, mesoscale, and synoptic mechanisms in triggering flood-producing rainfall. The main focal point of this study is the evaluation of the WRF Model's capability to reproduce such high-impact events. This evaluation includes sensitivity tests of different microphysics schemes and the examination of the evolution of convection characteristics using WRF-simulated radar reflectivity. In addition, the quantification of the relative contributions of different remote water vapor sources was examined utilizing a back-trajectory analysis method.

2. WRF simulation designs and validations

a. WRF simulation setups

Two main sets of simulations are carried out using the WRF Model, version 3.6.1, to examine the J13 storm. The first set *S1* is conducted to examine the extent to which the J13 storm can be simulated by a state-of-the-art numerical model, with no data assimilation technique included. The evolution of modeled storm features (e.g., rain rate and rainfall characteristics) is validated against available observations and analysis data. A second set *S2* is performed to provide the large-scale circulation and the atmospheric parameters for a 10-day back-trajectory

TABLE 1. WRF Model description.

WRF	Version 3.6.1 Center located at 60°N, 114°W Grid spacing: <i>D1</i> : 3 km; <i>D2</i> : 9 km; and <i>D3</i> : 27 km Time steps: <i>D1</i> : 20 s; <i>D2</i> : 60 s; and <i>D3</i> : 180 s All domains: from ~140 m below the ground to up to 50 hPa (~20 000 m MSL) with 51 levels
Main input variables	Soil and air temperature, wind speed, soil moisture, atmospheric pressure, and RH
Simulation period	<i>S1</i> : from 1200 UTC 18 Jun to 0000 UTC 23 Jun 2013 (4.5 days); <i>S2</i> : from 0000 UTC 10 Jun to 0000 UTC 23 Jun 2013 (13 days)
Spinup period	~12 h
Input data's boundary conditions	Reanalysis: ERA-Interim
Some physics schemes	
Microphysics	<i>S1</i> : WSM6, Thompson scheme, Morrison 2-moment scheme, and WDM6; <i>S2</i> : WDM6
Long- and shortwave scheme	RRTM for longwave and Goddard for the shortwave radiation
Surface layer	Eta similarity
Land surface	Noah LSM
Planetary boundary layer	Mellor–Yamada–Janjić scheme
Cloud or cumulus parameterization	Betts–Miller–Janjić scheme for <i>D2</i> and <i>D3</i>
Lake and urban physics	Not considered in these runs

analysis. The second set is conducted by nudging the internal and boundary values toward those values produced by the forcing analysis at 6-h intervals. This approach forces WRF to correctly simulate the synoptic-scale circulation and the finescale thermal dynamical fields several days before the flooding. NCEP Final (FNL) analyses (NOAA/NWS/NCEP 2000) with 6-hourly and 1° grid spacing are used to provide the initial and boundary conditions for both *S1* and *S2*. Details of the WRF Model setup are given in Table 1. Specifically, model physics modules that are common to both sets of simulations are the Rapid Radiative Transfer Model (RRTM) longwave radiation scheme, Goddard shortwave radiation scheme, Eta similarity for surface layer parameterization, Mellor–Yamada–Janjić scheme for planetary boundary layer parameterization, and the Betts–Miller–Janjić scheme for cumulus parameterization within the coarse-grid domain (the second domain *D2* and first domain *D3* in Fig. 1, with resolutions of 9 and 27 km, respectively). Four microphysics parameterization schemes, including the WRF single-moment 6-class microphysics scheme (WSM6), the Thompson scheme, the Morrison 2-moment scheme, and the WRF double-moment 6-class microphysics scheme (WDM6) are tested in *S1* to find out which one best simulates this event. In *S2*, only the WDM6 is used.

The simulation domain for *S1* is shown in Fig. 1a. The model domain center for *S1* is located at 60°N, 114°W. For the three nested domains, the outer one (*D3*) has a grid spacing of 27 km, with 253 grid points in the east–west direction and 193 grid points in the north–south direction. The second domain has a grid spacing of 9 km, and the third domain *D1* has a grid spacing of 3 km. Convection is resolved in the inner domain. A similar configuration with the same *D1* and *D2* but a much larger outer domain is used for *S2* (Fig. 1b), which extends farther south to 10°N

to include all the potential moisture sources, such as the Gulf of Mexico, for the long-period back-trajectory analysis. For *S1* and *S2*, the vertical levels are set to 51 with the model top at 50 hPa. The first set is initiated at 1200 UTC 18 June 2013 and integrated for 4.5 days, whereas *S2* is initiated at 0000 UTC 10 June and is integrated for 13 days. The time steps for *D1*, *D2*, and *D3* are set to 20, 60, and 180 s, respectively, for both *S1* and *S2*.

The purpose of the *S1* simulation is to reconstruct the evolution of the convection systems and the related three-dimensional thermodynamic environment for this event, as well as to allow analysis of the evolution of the convective/stratiform precipitation components. The purpose of conducting the *S2* simulation is to provide the large-scale circulation field, the atmospheric water content, and surface evaporation and evapotranspiration parameters in a much larger domain for a much longer period, and these variables will be used for the back-trajectory analysis. The main focus of the back-trajectory analysis is to determine the moisture sources affecting the flooding region (the blue box in Fig. 2a). The exact evolution of the MCSs within the flooding region is not the concern of *S2*. Overall, the objectives of simulations *S1* and *S2* are different and the simulated precipitation within the flooding region may not necessarily be comparable. However, the large-scale circulation patterns do look similar when *S2* overlaps with *S1* (from 1200 UTC 18 June to 0000 UTC 23 June).

b. Validation datasets

Precipitation is the end product of complex and intricate interplays between a myriad of atmospheric processes and environmental features that occur over a wide spectrum of scales. It is also one of the most difficult variables to simulate accurately in a model. The fidelity of

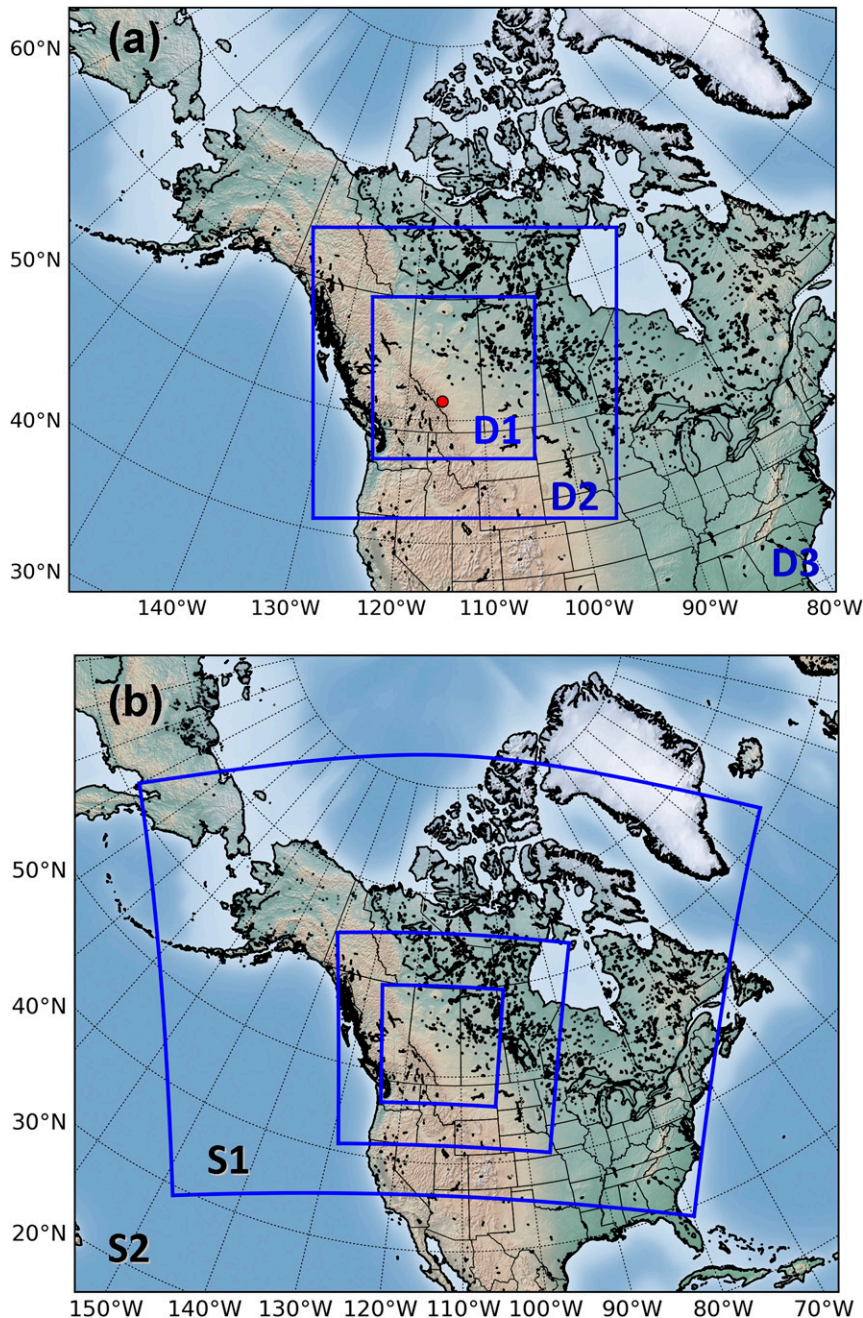


FIG. 1. (a) WRF domain setup for S1. The inner domain (i.e., D1) has a resolution of 3 km. The outer domains (i.e., D2 and D3) have a resolution of 9 and 27 km, respectively. (b) WRF domain setup for S2 compared with S1. The red dot in (a) represents where flooding happened.

the model precipitation often gives a good indication of the overall accuracy and quality of the simulation. The model results are validated through a comparison between simulated and observed precipitation.

Station gauge data from the Alberta Agriculture and Forestry archive (<http://agriculture.alberta.ca/acis/alberta-weather-data-viewer.jsp>) were used to validate the

WRF-simulated precipitation at specific locations near the foothills where strong and persistent orographically forced rainfall was observed. The Canadian Precipitation Analysis (CaPA) product developed by Environment Canada (now Environment and Climate Change Canada; Mahfouf et al. 2007) was used to evaluate the domain-averaged precipitation rate from the WRF simulations.

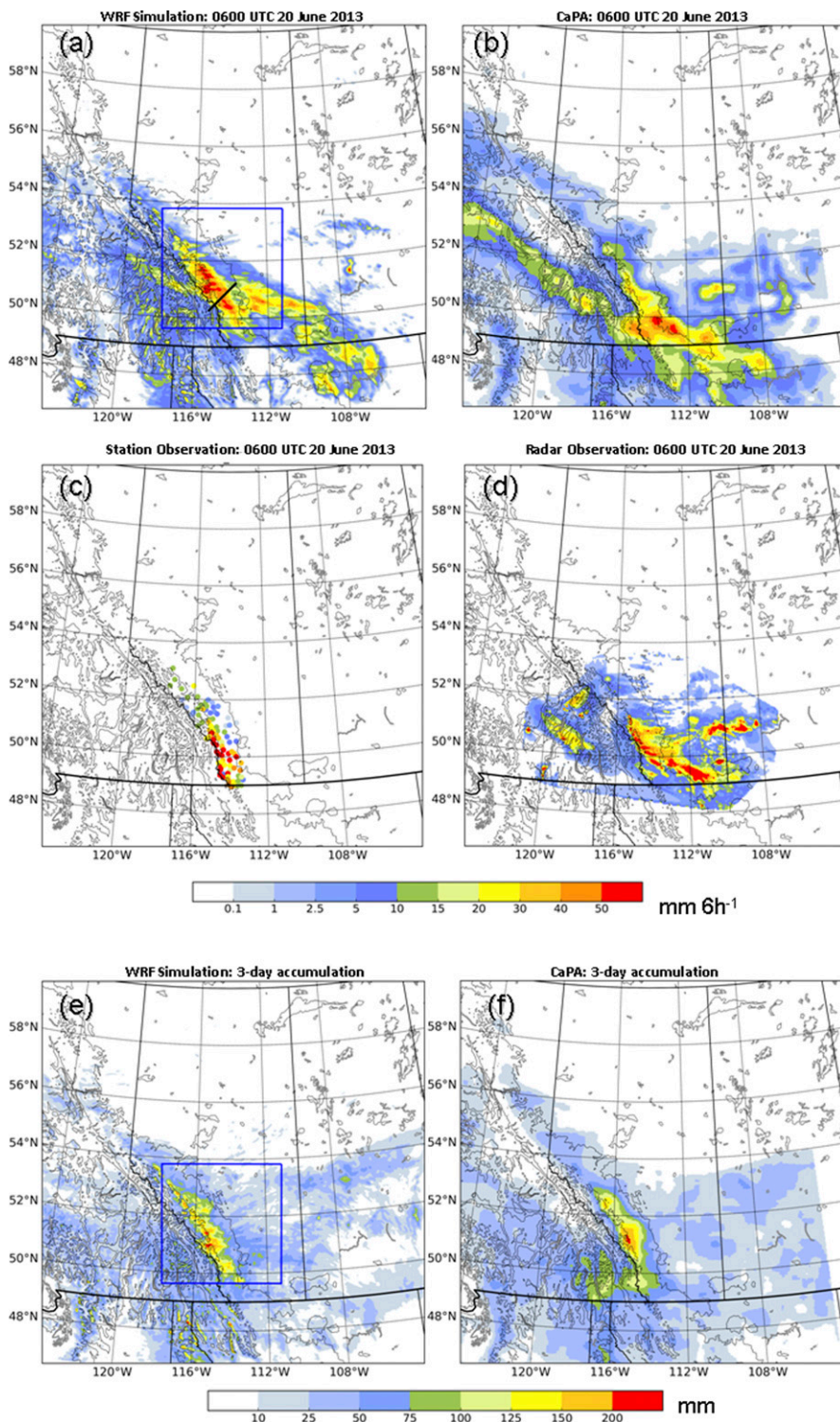


FIG. 2. (a) WRF simulation using WDM6, (b) CaPA, and (c) station- or (d) radar-observed 6-h averaged rain rate. In (a)–(c), results are at 0600 UTC 20 Jun 2013. (e) WRF simulation using WDM6 and (f) CaPA 3-day accumulated precipitation for the period from 0000 UTC 19 Jun to 0000 UTC 22 Jun 2013. Topography is contoured every 1000 m above 1 km MSL (starting from $z = 2$ km MSL). Black contours indicate provincial boundaries.

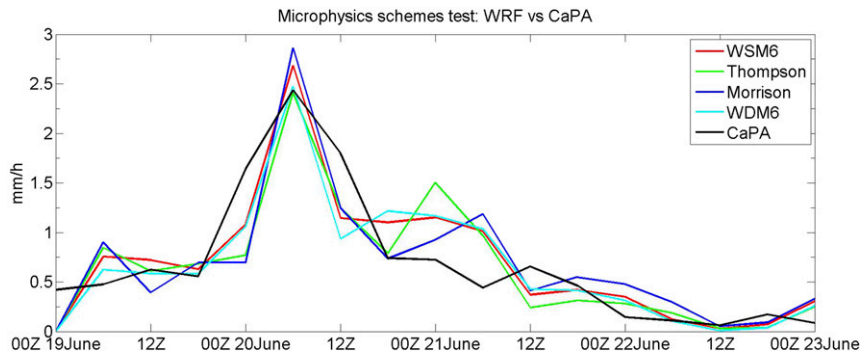


FIG. 3. WRF-simulated 6-h precipitation rates (mm h^{-1}) with different microphysics schemes (WSM6, Thompson, Morrison, and WDM6) compared with CaPA. The precipitation rates were averaged over the flooding region as shown in Fig. 2a (blue box), starting from 0000 UTC 19 Jun 2013.

CaPA assimilates all the available radar and station observations, as well as operational model forecast output to produce the best surface precipitation estimate at 6-h intervals and at 10-km spatial resolution. Besides that, hourly rain-rate data from Environment Canada's operational radar network (Joe and Lapczak 2002) were also used to qualitatively evaluate the evolution of mesoscale convective systems before and during the flooding. Radar rainfall rates were estimated from constant-altitude plan position indicator (CAPPI) reflectivity composites at 2.5 km above mean sea level (MSL), combining data from the Carvel (WHK; location 53.56°N , 114.14°W ; elevation 766 m) radar near Edmonton in Alberta, Strathmore (XSM; location 51.21°N , 113.40°W ; elevation 967 m) radar near Calgary in Alberta, Schuler (XBU; location 50.31°N , 110.20°W ; elevation 863 m) radar near Medicine Hat in Alberta, and Silver Star Mountain (XSS; location 50.37°N , 119.06°W) radar near Kelowna in British Columbia.

Figures 2a–d show the rain rate produced by the WRF simulation, CaPA, the station observations, and radar data at the peak of the precipitation the night before flooding occurred, respectively. Since CaPA data are only available every 6 h, the rain rates from the other sources were averaged over 6 h to make them comparable to CaPA precipitation. The peak precipitation produced by the WRF simulations (Fig. 2a) is located slightly north when compared with the CaPA product (Fig. 2b) and radar observations (Fig. 2d).

Comparisons of the spatial distributions of the 3-day (from 0000 UTC 19 June to 0000 UTC 22 June 2013) accumulated precipitation between WRF and CaPA are shown in Figs. 2e and 2f. As can be seen, most of the WRF precipitation is concentrated along the eastern slopes and foothills of the Rockies, which is consistent with station rain gauge measurements (Fig. 2c) and CaPA precipitation (Fig. 2f). Both WRF and CaPA precipitation show

maxima around 51°N , 115°W , which is upstream of where the flooding occurred. The WRF-simulated precipitation pattern shows significant finescale structures related to the local terrain, indicating that it was mainly orographically generated precipitation. The CaPA precipitation, which mainly comes from the interpolation of observations, shows a similar precipitation distribution but with coarser resolution compared with gauge observations. Figure 3 compares the time series of CaPA and WRF-simulated precipitation rates averaged over the flooding region. The spatial distributions of accumulated precipitation and the time series of domain-averaged rain rates simulated by WRF both show reasonable agreement with the available observations.

c. Sensitivity tests of microphysics and land surface schemes

Two sets of sensitivity experiments are conducted using the S1 base configurations. In the first set, different options for the model microphysics scheme are chosen to examine the sensitivity of the model rainstorms to the selected scheme and to provide guidance on which option can best reproduce the observed precipitation through a quantitative evaluation using the equitable threat score (ETS; Brill and Mesinger 2009). Results from these experiments provide insights into the roles of the different microphysics processes in producing the observed rainfall during the flood.

Specifically, four microphysics schemes were selected for sensitivity tests, including WSM6 (Hong and Lim 2006), Thompson (Thompson et al. 2008), Morrison 2-moment scheme (Morrison et al. 2009), and WDM6 (Lim and Hong 2010). The simulated 6-h precipitation rates averaged over the flooding region for these schemes are shown in Fig. 3. In general, all four WRF simulations reproduce precipitation rates reasonably close to the CaPA rain rates; both the general evolution and the peak

are well represented. However, the model produced a secondary peak near 0000 UTC 21 June, which does not appear in CaPA. A careful comparison between CaPA, the WRF simulation, and radar observations has been conducted. It is possible that CaPA missed some convective cells generated near the eastern slope in the southern part of the domain as well as some convective bands extending farther east. These appear in both the WRF and radar products and also likely contributed to this secondary peak in the domain-averaged rain rate. The double-moment microphysics schemes show reduced area-averaged rain rates that match the CaPA results better. Since all four microphysics schemes produce domain-averaged rain rates slightly higher than CaPA, it is possible that CaPA underestimates the actual rain rate.

There are several popular metrics that can be used to evaluate the WRF Model performance in simulating a severe precipitation event. Some simple performance measures include correlation coefficient, frequency bias, probability of detection (POD), and ETS. The frequency bias calculates the ratio of the number of forecasts to the number of observations of the event. POD calculates the ratio of the points that are both forecasted and observed to the number of observations of the event (Brill and Mesinger 2009). ETS includes information from both the frequency bias and the POD, and it is easier to calculate than the objective-based methods. Both the frequency bias and the ETS were selected to quantitatively evaluate the results from the four different microphysics schemes.

WRF-simulated rain rates were first interpolated to station locations, as shown in Fig. 2c. The calculated correlation coefficients between WRF simulations and station observations for the accumulated rainfall from 0000 UTC 20 June to 0000 UTC 21 June 2013 are 0.64, 0.62, 0.43, and 0.32 for Morrison, WSM6, WDM6, and Thompson, respectively. This indicates moderate (>0.3) to strong (>0.6) correlation between simulations and observations (with 95% significance).

The ETSs (Fig. 4a) were also calculated based on the results among all the available stations within the flooding region (Fig. 2c) for the same period. These calculations show reasonable values around 0.3 for precipitation thresholds higher than 45 mm day^{-1} for WDM6. Morrison, Thompson, and WSM6 also show relatively good values when the thresholds are higher than 70 mm day^{-1} . For thresholds lower than 70 mm day^{-1} , Thompson and Morrison schemes show mainly positive and some negative scores, whereas WSM6 gives very poor negative scores. Only WDM6 shows consistently good scores for different thresholds from 45 to 100 mm day^{-1} , reaching as high as 0.45 for the 90 mm day^{-1} threshold. For thresholds less than 25 mm day^{-1} , ETS values converge

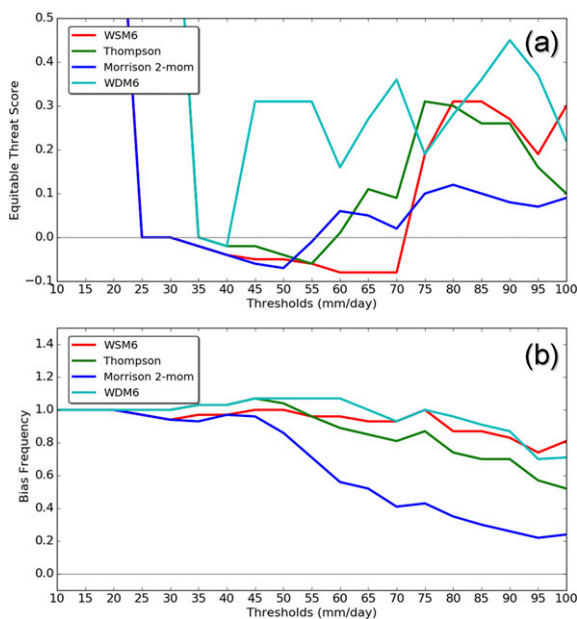


FIG. 4. Comparison of (a) ETS and (b) bias frequency at different precipitation rate thresholds (mm day^{-1}). Lines with different colors show the corresponding ETS values for different microphysics schemes. Both ETS and bias frequency values are calculated by interpolating WRF-simulated rain rates to the locations of those stations shown in Fig. 2c and then comparing with station observations for a 24-h time frame from 0000 UTC 20 Jun to 0000 UTC 21 Jun. ETS for thresholds less than 25 mm day^{-1} are close to 1 (not shown). Bias frequency with a value less than 1 indicates that WRF-simulated precipitation rates are in general lower than that of the rain gauge measurement.

to 1 for all four schemes (not shown), indicating that lower thresholds may not be effective in evaluating the performance of these microphysics schemes. Considering that the highest rain rate is approximately 50 mm h^{-1} (Fig. 2c) at 0600 UTC 20 June 2013 and that these intense rates were maintained for $<6 \text{ h}$ (as indicated in Figs. 2, 3), the precipitation threshold range from 50 to 100 mm day^{-1} in Fig. 4a should be more representative in evaluating model performance. Bias frequencies (Fig. 4b) with values less than 1 for thresholds higher than 50 mm day^{-1} indicate that WRF-simulated precipitation rates are in general lower than that of the rain gauge measurements. Again, WDM6 shows better scores than the other schemes, especially for thresholds higher than 50 mm day^{-1} . Since WDM6 performs better compared with the others in general, it was selected for all subsequent simulations.

An interesting point is that all three double-moment microphysics schemes show much better ETSs than the single-moment scheme for thresholds less than 75 mm day^{-1} . This may be partially attributable to using double-moment schemes that are better at simulating stratiform precipitation that has lower intensity compared

with convective precipitation (Bryan and Morrison 2012). Single-moment schemes tend to overestimate rain rates because of their inadequate representation of liquid and ice microphysics (Viterbo et al. 2016).

In a second set of evaluations, WRF with WDM6 was coupled with different land surface models (LSMs) to evaluate the sensitivity of model storm precipitation to the use of different LSMs. In particular, the Noah (Ek and Mahrt 1991), CLM (Oleson et al. 2004), and RUC (Smirnova et al. 1997, 2000) LSMs were tested. A comparison between CaPA-assimilated and WRF-simulated precipitation rates, averaged over the flooding region, showed that the rainfall amounts were not significantly different between these simulations (not shown). A possible explanation is that large-scale disturbances, especially if associated with strong moisture convergence, may result in land surface processes becoming less important in determining precipitation rates (LeMone et al. 2008; Smith et al. 2013). Hence, the LSM sensitivity test results here do not suggest that a specific LSM is significantly superior to others. The Noah LSM is used in the following WRF simulations.

3. WRF-simulated synoptic conditions and precipitation characteristics

An overview of the large-scale circulation and environmental conditions of the J13 storm based on the WRF simulations is presented in this section. Qualitative validations of the evolution of the convective systems are then presented to assess how well the evolution of the observed precipitation features was reproduced in the simulation. The evolution of storm characteristics and the relative contributions of convective and stratiform precipitation at different stages of the J13 event are also discussed.

a. Event description and synoptic developments

In this section, the WRF Model-simulated synoptic and mesoscale conditions are examined to validate whether the simulation accurately captured key controlling weather features associated with the J13 event, and to illustrate the convective processes that could not be observed by the relatively coarse observational network.

The development of the antecedent large-scale atmospheric flow pattern up to 2 weeks prior to this event has been examined by Milrad et al. (2015). It was found that a train of Rossby waves across the North Pacific Ocean helped to form a blocking pattern in the northeastern North Pacific. A detailed analysis of the evolution of weather patterns during the heavy precipitation period can be found in Liu et al. (2016). It was shown that a slow-moving upper low with an associated surface low pressure system moved into southern Alberta, which, combined with terrain effects,

brought continuous precipitation during the period 19–21 June 2013, especially over the foothills and mountains.

At 0000 UTC 20 June 2013, the simulation (Fig. 5a, 200 hPa) shows a deep, negatively tilted shortwave trough along the Pacific coast with a closed upper low centered over western Washington. An upper ridge is observed to the east of the trough extending from central Alaska toward the U.S. Great Plains. The locations of the upper trough and ridge are consistent with the evolution of the system discussed in Liu et al. (2016). The simulation also captures observed strong jets upstream and downstream of the trough. At 500 hPa (Fig. 5b), the trough and ridge locations are similar to those at 200 hPa (Fig. 5a), with a strong diffluent flow over southern Alberta. A closed cyclone developed over Washington State and is shown at 700 hPa (Fig. 5c). At 850 hPa, quasi-stationary synoptic conditions (dipoles of high and lows) over north-central Canada, southern Alberta, and Montana allowed for the development of enhanced low-level easterly flows across the Canadian Prairies into the Rockies (Fig. 5d). Fast-moving moist air, with velocities greater than 15 m s^{-1} at the 850-hPa level, oriented nearly perpendicular to the mountain range, provided a sufficient moisture supply. The jet slowed down as the core of humid air reached the eastern slopes (located around 114°W) with high temperatures $>20^\circ\text{C}$. The blocking effect of the mountains helped to concentrate the precipitation over a relatively small region (Fig. 2a). The heaviest rainfall occurred south of the axis of the highest 850-hPa winds (Figs. 5d, 2a–d) and coincides with the region of the highest 850-hPa equivalent potential temperature (not shown). The warm, moist, unstable air advected by the low-level easterlies impinged on steep terrain, which produced on average more than 100 mm of rain within 3 days (19, 20, and 21 June; Figs. 2e,f).

The thermodynamic environment (Figs. 6, 7) over the foothills of the Rockies is examined using WRF sounding profiles and temporal variations of some of the most representative thermodynamic variables. The location of the selected sounding is 51°N , 114°W , one of the sites where subsequent flooding occurred. The nearest observed sounding was by aircraft taken during ascent from Calgary International Airport (51.1°N , 114°W) at 2356 UTC 19 June 2013 (Fig. 6b). Although the aircraft sounding is somewhat north, about 1 h later, and without dewpoint temperature data, the comparison shows that the two vertical temperature profiles are similar, with both capturing strong easterly/northeastern winds in the boundary layer. The WRF sounding at 2300 UTC 19 June (Fig. 6a) exhibited strong instability (high buoyancy) below 2000 m MSL with a CAPE value of 1252 J kg^{-1} . Specific humidity was more than 9 g kg^{-1} at 850 hPa (Fig. 5d), with the atmosphere nearly saturated.

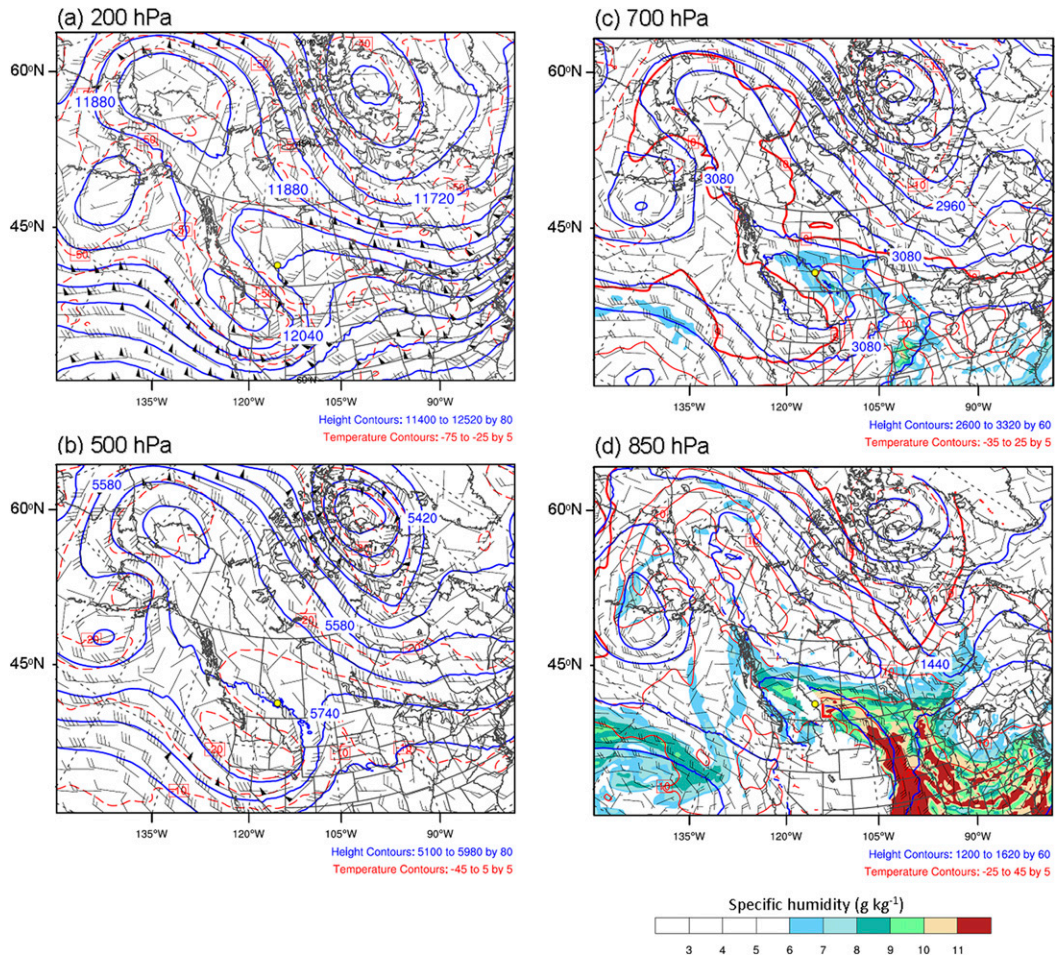


FIG. 5. Large-scale circulation at (a) 200, (b) 500, (c) 700, and (d) 850 hPa at 0000 UTC 20 Jun 2013. Isohyse for geopotential height is in blue contours. Isotherms for temperature are in red contours. Wind barbs are the black vectors (knots). Specific humidity (g kg^{-1}) is in color. The location of Canmore, Alberta, at 51°N , 115.4°W is highlighted by the yellow dot. An 850-hPa low pressure center is highlighted as a red “L” in (d).

The relative humidity (RH; Fig. 7a), at location 51°N , 115.35°W , which is farther west and closer to the heavy precipitation region, shows in general RH greater than 90% within 1000 m above ground level (AGL) from 1200 UTC 18 June to 1200 UTC 21 June. Especially around 0000 UTC 20 June, the atmospheric RH is $>80\%$ up to 9 km AGL, which indicates that the entire troposphere was mostly saturated. The temporal variation of RH is consistent with the change of the column integrated water vapor (IWV) amount at the same location (Fig. 7c). RH is substantially reduced to almost zero around 1200 UTC 21 June, indicating that the flow pattern changed. The low RH is because of a new air mass in the area at that time where the moisture source was cut off. IWV also drops to nearly zero around that time (Fig. 7c). The vertical rate of change of equivalent potential temperature θ_e (Fig. 7b) represents the potential instability of a layer and is often used as a diagnostic for the possibility of convection due

to layer uplifting. In general, θ_e increases with altitude in the atmosphere in stable conditions. In this case, there is potential instability below 4000 m AGL for much of the 24-h period from 0000 UTC 19 June to 0000 UTC 20 June (Fig. 7b). The time series of CAPE (Fig. 7c) shows a value close to 1000 J kg^{-1} around 0000 UTC 20 June, indicating strong instability just before significant precipitation began. This is consistent with the changes of rainfall rate (Figs. 3, 7c) that show increasing precipitation intensity from 0000 UTC 19 June to 0000 UTC 20 June and reaching a peak around 0000 UTC 20 June. The moist low-level easterly jet experienced orographic lift as it reached the foothills, which increased instability leading to condensation and heavy rainfall along with significant convection (Figs. 2a, 7). After this convective rainfall, the atmosphere stabilized between 0000 and 1200 UTC 20 June, and there was a corresponding decrease in precipitation intensity (Figs. 7b,c). Compared to three previous

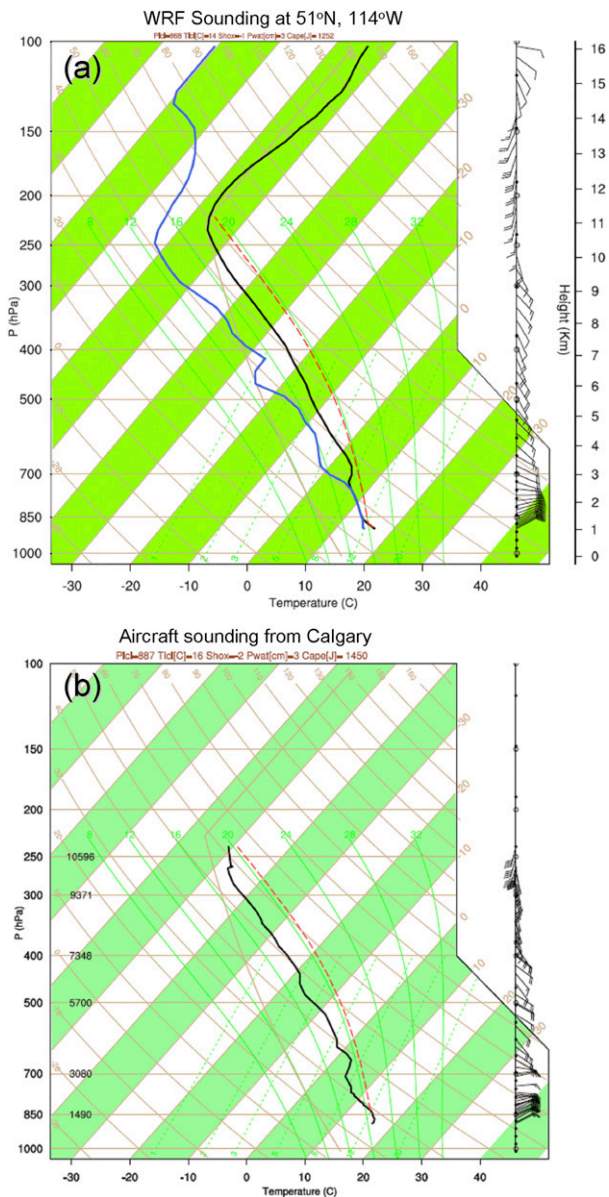


FIG. 6. (a) Sounding profile taken from 51°N, 114°W at 2300 UTC 19 Jun 2013 from the WRF simulation. The sounding location is highlighted as the red dot in Fig. 1. (b) Aircraft sounding taken from Calgary airport (51.1°N, 114°W) at 2356 UTC 19 Jun 2013. Note that the aircraft sounding has no dewpoint temperature data.

significant flooding events that occurred in 1965, 1973, and 1982 in Alberta (Liu et al. 2016), the storm environment was much warmer and very convectively unstable, with CAPE values substantially higher.

b. Comparison between simulated and observed precipitation structures

As shown above, the WRF-simulated precipitation shows reasonable agreement with the available

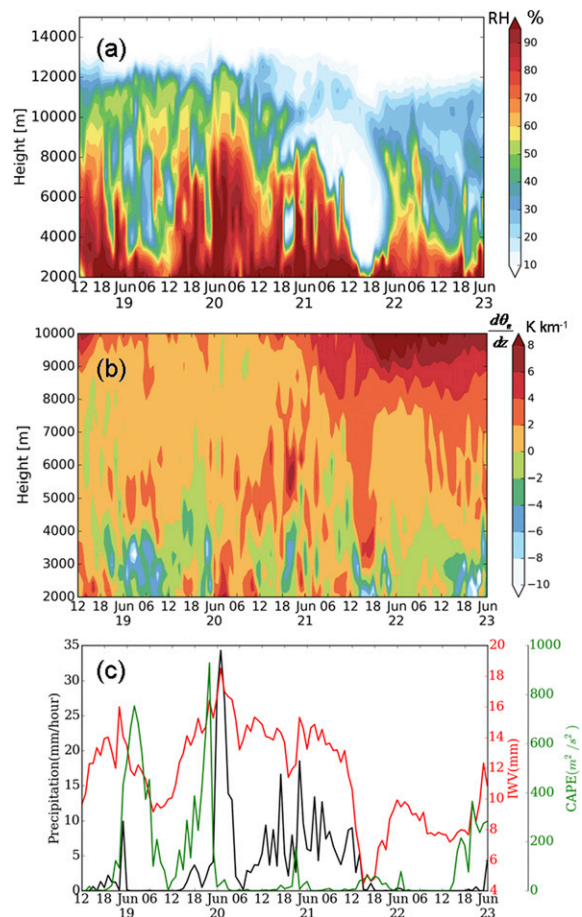


FIG. 7. WRF-simulated time series of (a) RH; (b) $d\theta_e/dz$; and (c) precipitation, column IWV, and CAPE at the location (51°N, 115.35°W) from 1200 UTC 19 Jun to 0000 UTC 23 Jun 2013. Time is labeled every 6 h. The y-axis height is in meters above mean sea level.

observations. Radar reflectivity comparisons between the hourly radar reflectivity output from WRF and radar observation are shown in Fig. 8. The strongest convection occurred during the night of 19 June over southern Alberta, producing 50 mm h⁻¹ rain with radar reflectivity around 50 dBZ over a narrow swath of the foothills (Figs. 2a, 8a–d). The strong upslope flow of moist air, together with a series of embedded intense convective complexes, contributed to the flooding. The convective cells reformed repeatedly near a fixed location over the foothills and the eastern slopes (Figs. 8a–d). Narrow southwest–northeast-aligned mesoscale precipitation bands associated with a peak radar reflectivity of 50 dBZ appeared in both the WRF simulation and radar observations in the region east of the foothills. This occurred for a short time period during the convective phase in which the maximum observed accumulated precipitation was reported near the foothills in the observations

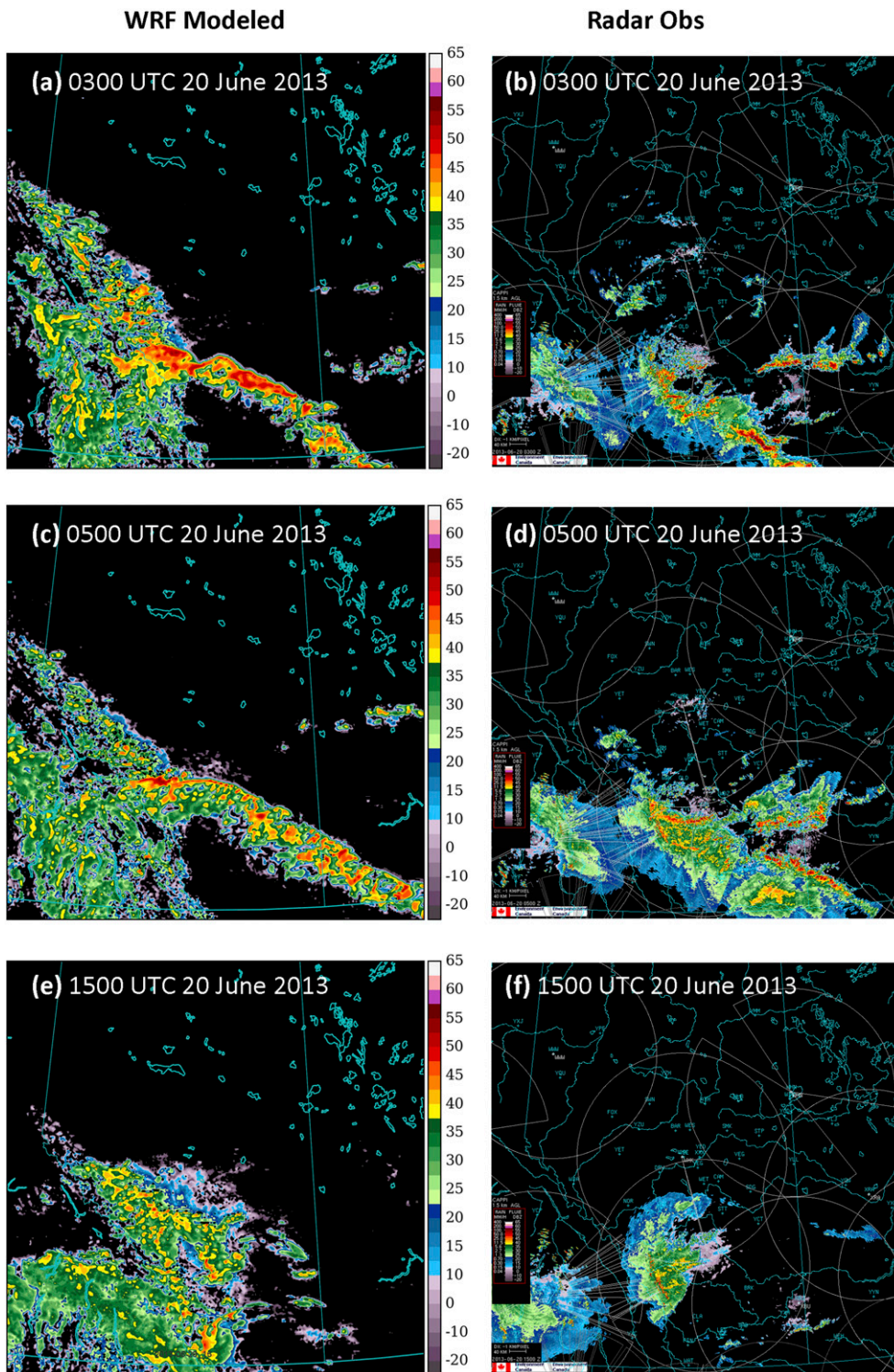


FIG. 8. WRF-simulated simulated radar reflectivity (dBZ) vs radar composite CAPPI reflectivity at 2.5 km MSL at (a),(b) 0300 UTC; (c),(d) 0500 UTC; and (e),(f) 1500 UTC 20 Jun 2013. Blue lines highlight the provincial boundaries and locations of lakes.

(Figs. 2e,f). The red/yellow cores in WRF-simulated reflectivity and radar-observed reflectivity greater than 40 dBZ indicated convective precipitation areas (Figs. 8a–f). Similar banded precipitation features were simulated by WRF with various differences in the exact locations and characters of the precipitating system. For example, the WRF Model shows a linear characteristic extended from the foothills to the southeastern domain edge, whereas the radar observation shows smaller features oriented along the terrain with some smaller embedded linear features extending to the southeast. These banded structures are different; the model does not seem to capture the character of the precipitating system very well (Figs. 8d–f). Along the line to the southeast, a cellular appearance is shown in the WRF Model (Fig. 8c); however, short sections of linear banded convective regions are presented in the radar observation (Fig. 8d). Besides the location inconsistency, the model also appears to predict the onset of heavy precipitation, albeit a few hours too early.

The vertical cross sections of WRF-simulated radar reflectivity are shown in Fig. 9 for 0100, 0800, and 1200 UTC 20 June from XSM over Burns Creek. The location of the cross section is highlighted as a thick black line in Fig. 2a. At 0100 UTC (Figs. 9a,b), radar reflectivity showed a deep convective cell over the eastern slopes of the Rockies with the echo top extending well above 10 km AGL. At 0800 UTC (Fig. 9c), the radar-observed melting layer is evident as a thin layer about 50 dBZ between 2.0 and 2.5 km. The vertical cross section at 1200 UTC (Figs. 9e,f) shows a more widespread stratiform profile, which corresponds well with the horizontal pattern of radar reflectivity at 1500 UTC (Figs. 8e,f). However, the vertical structure of the convection was not well simulated by the model in general. The intensity is much stronger and the convection is deeper than the observations.

A conventional convective/stratiform separation algorithm was applied to investigate storm characteristics during the life cycle of the flood (Fig. 10). For a specific location with precipitation detected at the surface, if reflectivity of 40 dBZ or more is found in the vertical column over the surface, and if the height of the 7-dBZ level above this threshold is determined to be higher than 4 km, then the precipitation at that time and location is marked as convective (red areas in Figs. 10b,d). Areas with surface rainfall not meeting these criteria are deemed stratiform (Steiner et al. 1995). For example, in Fig. 8, precipitation with less intensity surrounding the anvil (green/blue area) was identified as stratiform precipitation. Figure 11 shows the relative contributions from convective and stratiform precipitation at different stages of the event. The convective activity was dominant at the beginning of the event, followed by relatively steady stratiform precipitation during the later stages. The

transition to stratiform dominant rainfall started around 0600 UTC 20 June (Fig. 11) when the convective precipitation decreased significantly. Note that stratiform precipitation did not noticeably increase at 0600 UTC 20 June, but instead became the dominant precipitation type because the convective precipitation decreased at this time. This indicates that the orographic lifting associated with the easterly winds both generated new convective cells and sustained widespread stratiform precipitation along the foothills of the mountains during the event.

A more detailed analysis of the precipitation and radar observations for the J13 event is given in Kochtubajda et al. (2016), who found a coupling between warm-rain collision coalescence processes and ice processes during the night before the flooding, as well as a high frequency of lightning and the presence of hail.

c. Precipitation mechanisms

Both observed (Figs. 2b–d,f) and simulated precipitation (Figs. 2a,e) show that the main feature in the J13 storm was the enhanced quasi-linear precipitation structures that were roughly aligned parallel, but with a slight angle, to the foothills. In addition, the strong low-level easterly flow that developed during 19 June (Liu et al. 2016) facilitated enhanced moisture transport toward the foothills. These results suggest that the orographic lifting of the strong easterly flow could have played a critical role in producing the precipitation.

The behavior of the airflow approaching a mountain barrier is determined by the nondimensional Froude number $Fr = U/(Nh_m)$ (Lin et al. 2001), where U is the barrier-normal component of the flow, N is the Brunt–Väisälä frequency, and h_m is the maximum terrain height. When $Fr \gg 1$, the flow can easily rise over the barrier, whereas nonlinear effects such as blocking or damming become important when $Fr < 1$. For the airflow approaching the foothills at 2300 UTC 19 June, that is, just before the onset of the heaviest rainfall, Fr can be estimated for the layer between the surface and the top of the mountains (between 900 and 800 hPa in Fig. 6). Within this layer $N \sim 7 \times 10^{-3} \text{ s}^{-1}$, $U \sim 12 \text{ m s}^{-1}$, $h_m \sim 1200 \text{ m}$, and Fr is estimated to be about 1.5. Effective uplift of the impinging flow was then facilitated because of the strong low-level jet (LLJ) and the relatively weak stratification. When moist effects are considered, the behavior of the moist impinging airflow is determined by the moist Froude number $Fw = U/(N_m h_m)$, where N_m is the saturated Brunt–Väisälä frequency (Durran and Klemp 1982). In fact, N_m was negative for conditions observed in the oncoming air (Fig. 7b, from 0000 to 0600 UTC 20 June), implying that the air was moist and absolutely unstable (Kirshbaum and Durran 2004). The existence of a moist, absolutely unstable layer is probably a reflection of

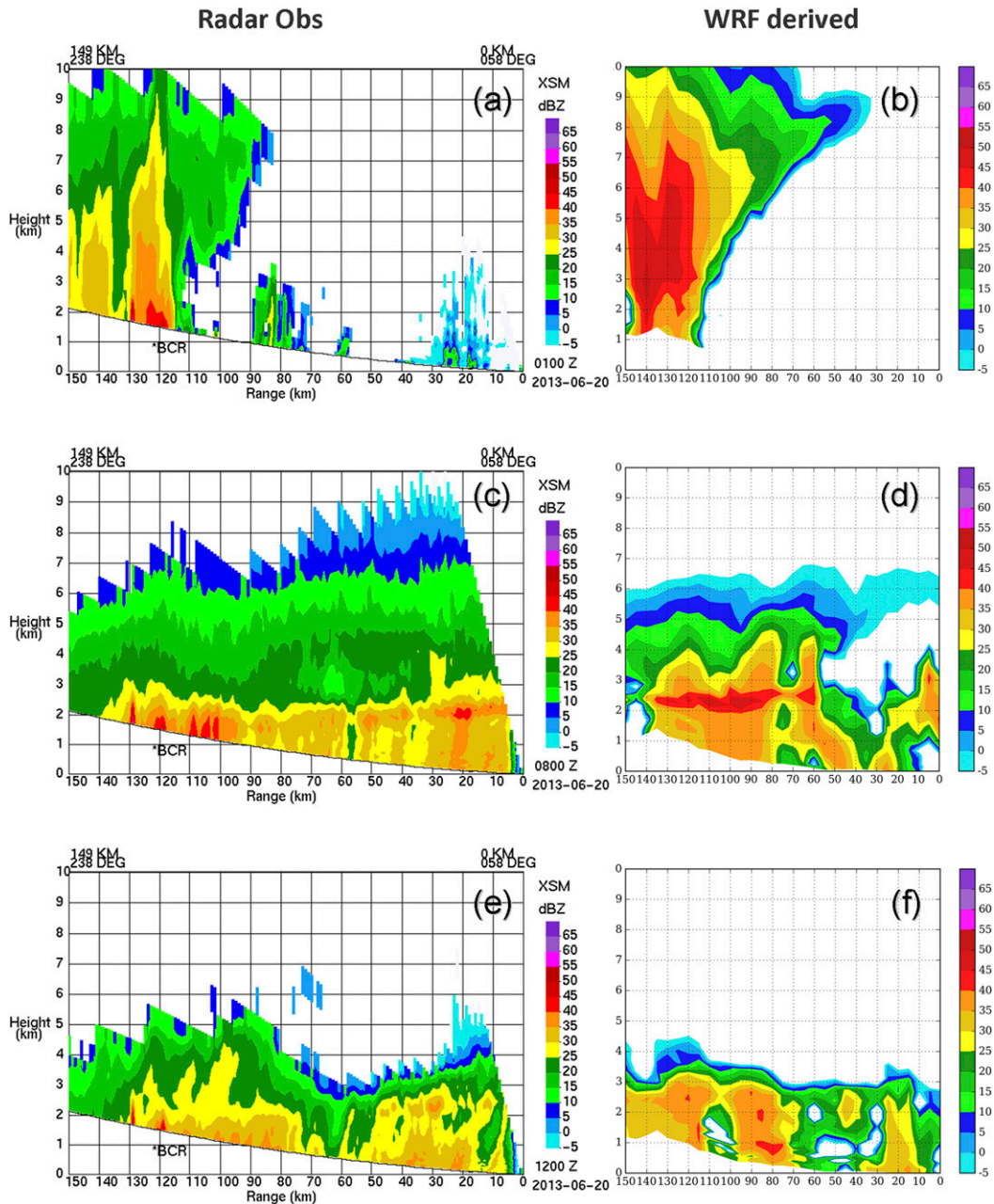


FIG. 9. Radar reflectivity cross sections from XSM over Burns Creek (BCR; 51.2°N, 113.4°W) vs WRF-simulated radar reflectivity (dBZ) at (a),(b) 0100 UTC; (c),(d) 0800 UTC; and (e),(f) 1200 UTC 20 Jun 2013. Cross sections are oriented along the 238° azimuth, starting at the XSM radar and extending to 150 km. The altitude is AGL relative to XSM with the elevation of 967 m. The location of the radar cross sections are highlighted as a thick black line in Fig. 2a.

dynamic lifting by the terrain in the model, but may also arise because the sounding was taken in a region of precipitation instead of from ambient environmental conditions. In summary, the conditions were highly favorable for the development of convective rainfall over the windward slopes, as is evident in both the observational and simulated results (Figs. 2a–d, 8a–f).

4. Moisture sources and transport

a. Water vapor budget analysis

Previous studies (e.g., Raddatz 2000) suggest that up to 35% of summer precipitation in the Canadian Prairies is derived from regional evaporation and evapotranspiration. On the other hand, some studies (e.g., Brimelow

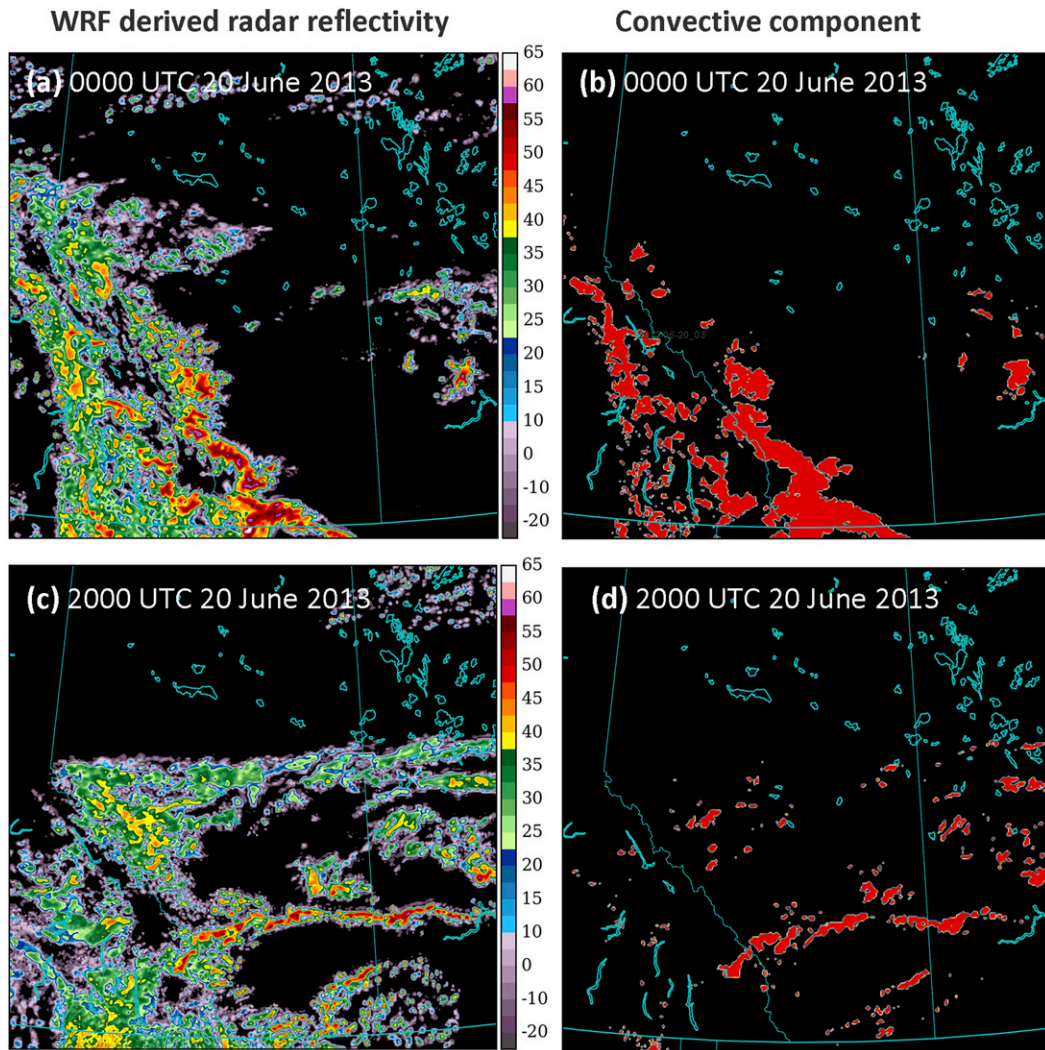


FIG. 10. WRF-simulated radar reflectivity at (a),(b) 0000 UTC and (c),(d) 2000 UTC 20 Jun 2013 before (left) and after (right) a convective/stratiform separation algorithm is applied. In (b) and (d), the areas marked in red represent areas with convective precipitation.

and Reuter 2005) point out that remote moisture sources such as the Gulf of Mexico could play an important role in providing the moisture for heavy orographic rainstorms that occurred in the northern vicinity of the J13 system. Here a water budget analysis was conducted for the flooding region (the region within the blue box highlighted in Fig. 2a) to assess the relative importance of regional evaporation, evapotranspiration, and external moisture influx in driving the J13 storm. Figure 12 shows the temporal changes of moisture fluxes across the four lateral boundaries (north, south, east, and west) of the flooding region. For the 4-day period before and during the flooding, moisture influx was dominated by horizontal advection from the eastern boundary, that is, from the Prairies side. The moisture transport was mainly

accomplished by the easterly low-level jet that developed over the southern Prairies during 19 June and hence was largely confined to the lower troposphere from 900 to 750 hPa.

Time series of area-averaged water budget components are presented in Fig. 13a. It is evident that the precipitation is closely balanced by the net lateral moisture flux. The lateral moisture influx through turbulence is not shown here but can be treated as the residual in Fig. 13a, and its contribution is less than 10% to the total precipitation. The local evaporation and evapotranspiration contributed less than 5% to the total precipitation, with the amount comparable to the change of the column IWV with time ($dIWV/dt$) within the flooding region. As can be seen, $dIWV/dt$ is very

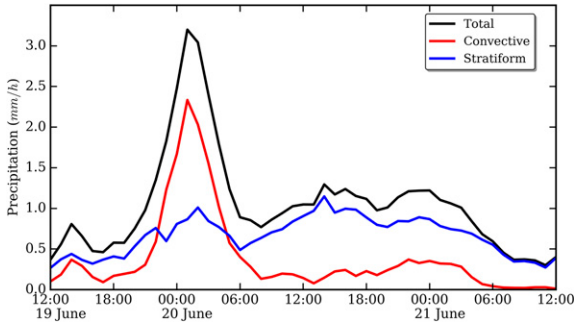


FIG. 11. WRF-simulated hourly rain rate (black curve) averaged over the flooding region (the blue box in Fig. 2a) during the flooding period, the relative contribution by convective precipitation (red curve), and stratiform precipitation (blue curve) after applying a conventional convective/stratiform separation algorithm using the WRF-simulated radar reflectivity.

small in this analysis but is large and positive when looking at a single point. In the time series in Fig. 7c, the IWV increases dramatically up to the time of the heavy rainfall. This can be explained from a local (Fig. 7) versus area-averaged perspective (Fig. 13a). Both local evaporation and evapotranspiration and $dIWV/dt$ show an obvious diurnal cycle over the U.S. Great Plains (Fig. 13b). Although playing a minor role in contributing to precipitation amounts, surface evaporation and evapotranspiration could still be essential through their role in changing the PBL buoyancy (Seneviratne et al. 2010).

The precipitation efficiency ϵ can be defined as the ratio of precipitation to net moisture influx (Doswell

et al. 1996). The results in Fig. 13 show that ϵ was very high and close to 1 for the 3-day period from 0000 UTC 19 June to 0000 UTC 22 June 2013. This is not surprising as both the terrain and the synoptic forcing provided effective lift for precipitation development, and the storm environment was moist, which minimized subcloud evaporative loss.

b. Methodology for back-trajectory analysis

Results from the water budget analysis suggest that the influx of external moisture is the primary source of moisture that fed the J13 storm. To quantify the sources of the water vapor that was advected into the region by the large-scale atmospheric circulation, the quasi-isentropic back-trajectory Hybrid Single-Particle Lagrangian Integrated Trajectory model (HYSPPLIT) developed by NOAA/Air Resources Laboratory, College Park, Maryland, was utilized. HYSPPLIT is a complete system for computing simple air parcel trajectories for complex dispersion and deposition simulations (Stein et al. 2015).

Hourly outputs from the 2-week (10–23 June 2013) WRF simulation S2 are provided to HYSPPLIT for the calculation of the back trajectories of the air parcels that contain water vapor. Hundreds of parcels are released above the surface from different locations over the flooding region right before the time when rainfall rate reaches its maximum (0000 UTC 20 June 2013; Fig. 2). The initial horizontal distribution of the parcels is assumed to be proportional to the distribution of the 6-h averaged rainfall at 0000 UTC 20 June 2013, and the vertical distribution is made proportional to the absolute humidity profile of the

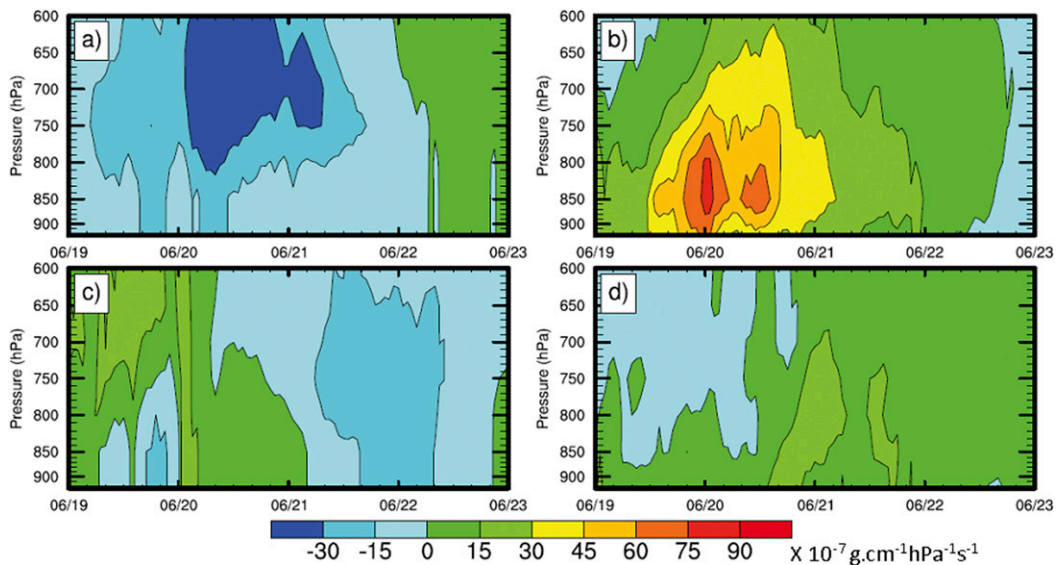


FIG. 12. Lateral water vapor flux from (a) west, (b) east, (c) south, and (d) north into the flooding region (the blue box in Fig. 2a) through horizontal advection.

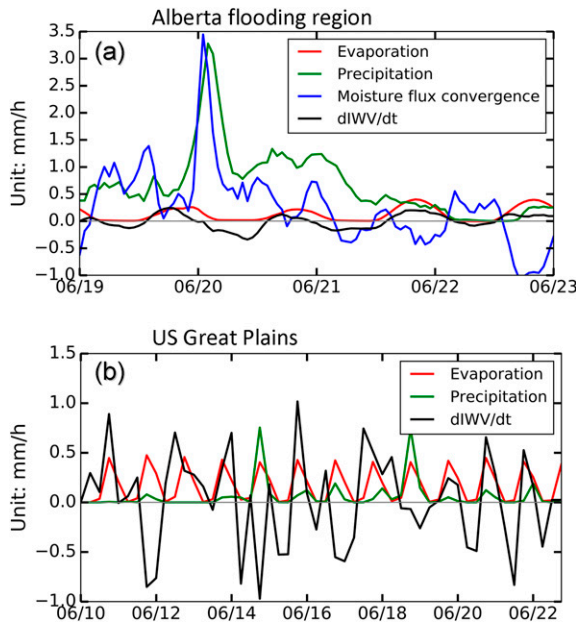


FIG. 13. (a) Contribution of precipitable water by lateral flux through advection integrated over the full depth of the atmosphere (blue curve), by surface evaporation and evapotranspiration (red curve), and by the change of the column IWV ($dIWV/dt$; black curve), compared with the total precipitation (green curve) within the flooding region (the blue box in Fig. 2a) during the flooding period. (b) The surface evaporation and evapotranspiration (red curve), the change of the column IWV ($dIWV/dt$; black curve), and the total precipitation (green curve) over the U.S. Great Plains (41.5° – 42° N, 103° – 98° W) for a 10-day period before and during the flooding.

air column about 3 h earlier. The back trajectories of these parcels are then calculated using HYSPLIT by advecting them backward in time. HYSPLIT uses the updated mean wind field from the WRF output at each time step together with a spread by a turbulent component. The trajectory information of each parcel (time and coordinates) for up to 10 days prior to flooding is then saved at 6-hourly intervals for later use. Examples of three back trajectories are shown in Fig. 14. Our results here (Fig. 14) are in general agreement with those of Liu et al. (2016) and Milrad et al. (2015), although different parcel tracking systems and different meteorological data were used in their studies. It is helpful to compare our results with theirs to examine the structural uncertainty in the back-trajectory analysis that is associated with the selection of the back-trajectory model and the meteorology background.

Taking an additional step, we use the trajectory information to track the water vapor content of the parcels by estimating the moisture uptake from the surface and loss through precipitation along the path (Stohl and James 2004). The procedure for this moisture tracking closely follows the methodology outlined in Sodemann

et al. (2008), with some modifications to utilize the output trajectory information from HYSPLIT in our study. The change of total water vapor within air parcel i backward in time is computed using the following equation:

$$q_{-(n-1),i} = q_{-n,i} \times (1 + \bar{f}_{-n,i}), \quad (1)$$

with $\Delta q_{-n,i} = q_{-n,i} \times \bar{f}_{-n,i}$, and $f_{-n,i} = (E_{-n,i} - P_{-n,i}) / IWV_{-n,i}$ for air parcel i .

A single time step is set to be 6 h, as we assumed that the atmospheric environment would not be significantly changed in 6 h and within the distance that the air parcel traveled. The calculation starts from time $t_0 = 0000$ UTC 20 June 2013, corresponding to $n = 1$ in Eq. (1). Parameter q_0 is then equivalent to the total amount of column IWV within the flooding region at time t_0 . Parameter q_{-1} ($= \sum_i q_{-1,i}$) is the total amount of water vapor that the air parcels carried at t_{-1} , 6 h before t_0 and so forth. Parameter Δq_{-1} ($= \sum_i \Delta q_{-1,i}$) is the total net moisture gain for all the air parcels at time t_{-1} at their locations calculated by the HYSPLIT trajectory analysis. Parameter \bar{f}_{-1} ($= \text{avg} \sum_i f_{-1,i}$) is the mean fractional contribution coefficient (Sodemann et al. 2008) at time t_{-1} averaged among all the air parcels, and $f_{-1,i}$ is the fractional contribution coefficient for air parcel i at time t_{-1} . Parameter $E_{-1,i}$ ($P_{-1,i}$) is the local evaporation and evapotranspiration (precipitation) at the location of the air parcel i at time t_{-1} . Parameter $IWV_{-1,i}$ is the column-integrated water vapor at this location, so $f_{-1,i}$ represents the water vapor change rate at this location at time t_{-1} , assuming that the change mainly comes from evaporation and evapotranspiration (gain) and precipitation (loss). If $E_{-1,i} > P_{-1,i}$, air parcel i gains moisture at time t_{-1} . If $E_{-1,i} < P_{-1,i}$, air parcel i loses moisture at time t_{-1} . Other factors, such as cloud condensation and precipitation reevaporation before it reaches the ground, are assumed to be secondary and ignored in Eq. (1) to simplify the calculation. The moisture gain and loss are assumed to be evenly distributed along the entire air column through vertical turbulent fluxes, so the change of IWV is not a function of height. In the calculation, variables E , P , IWV at time t_{-n} , and location of parcel i were read in from WRF S2 output. The calculated Δq at time t_{-n} and the location of parcel i were saved for the next step, which summarized the moisture uptake from all the paths to develop a geographic distribution so that the relative contributions from different remote source regions can be quantified.

The calculation starts from q_0 and continues until q_{-n} , with $t = -1, -2, -3, \dots, -n$, until $\sum_{x=1}^n \Delta q_{-x} > 0.95q_0$, at which time the calculation stops. This means that more than 95% of the moisture uptake happened within

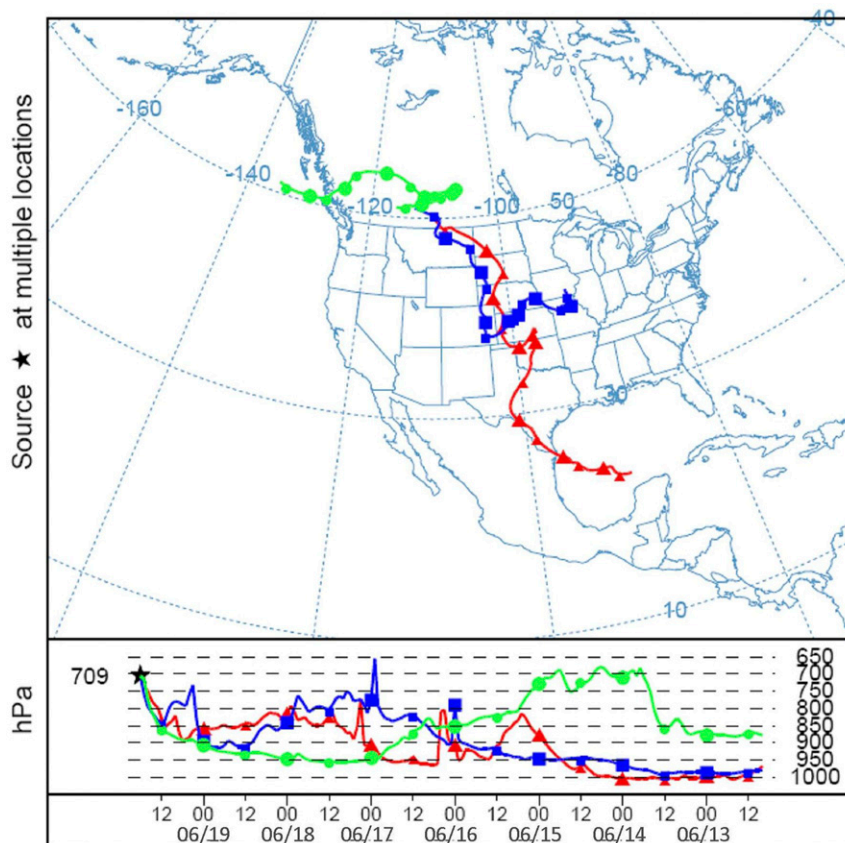


FIG. 14. NOAA HYSPLIT back-trajectory analysis tracing back to the water vapor source using WRF S2 simulation output. Backward trajectories end at 0000 UTC 20 Jun 2013. Three parcels released from the flooding region are shown here as examples. The parcels' locations and heights (hPa) in every 12 h are shown. The parcels' trajectories are traced back to 8 days prior to the event.

6n hours before t_0 , along the paths. At this point, further backward calculations along the trajectory for water vapor uptakes are no longer needed.

c. The remote moisture sources

The estimated moisture uptake along the paths of the air parcels during different periods before the flood event is shown in Fig. 15. The results show that the atmospheric moisture uptake for parcels that arrived at the flooding region within 1 day was mainly from the Canadian Prairies and the northern part of Montana and North Dakota (Fig. 15a). As discussed earlier, the easterly low-level jet (Figs. 5c,d) advected moisture toward the foothills, providing the immediate source for precipitation. Tracing back 3 days before the flooding, the uptake contribution from the southeast prairies, the U.S. Great Plains, and the Midwest became significant (Fig. 15b). It contributed at least half of the total moisture that was transported into the flooding region ~1–3 days later. Presumably, the moistening of the PBL

over the Canadian Prairies and U.S. Great Plains was mainly through surface evaporation and evapotranspiration. In June, local convection over the Great Plains and the Midwest is mainly diurnally phase locked (Li and Smith 2010). As can be seen in Fig. 13b, several days before the flooding, surface evaporation and evapotranspiration show magnitudes comparable to the diurnal variations of IWV, with little precipitation happening at the same time over the U.S. Great Plains. In Fig. 13b, the negative $dIWV/dt$ values during nighttime indicate the removal of the moisture from the U.S. Great Plains by the nighttime LLJ.

Tracing back 3–5 days before the flooding (Fig. 15c), the analysis shows that a significant amount of water vapor came from the southwestern United States, the North American monsoon region, and the eastern Pacific. The moisture was advected over the Sierra Nevada via an atmospheric river (Neiman et al. 2008; Liu et al. 2016) and was then transported northward by the Great Plains nocturnal low-level jet. The atmosphere follows a moist

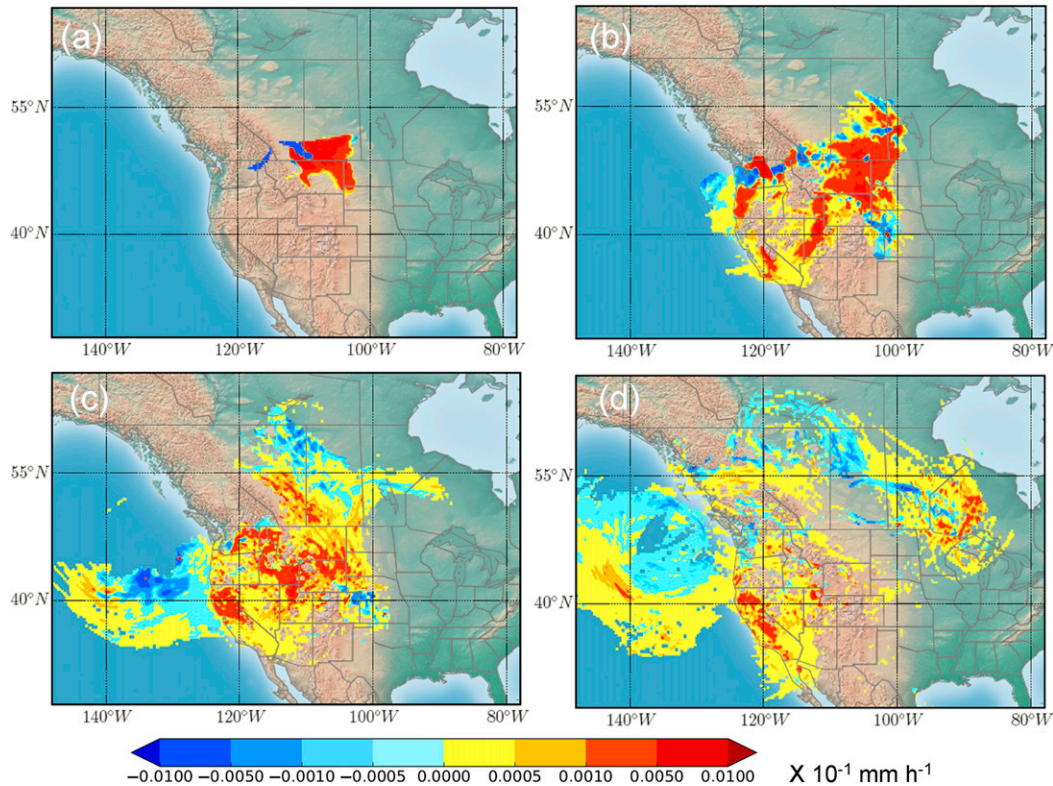


FIG. 15. Moisture uptake (a) between 6 h and 1 day, (b) 1 and 3 days, (c) 3 and 5 days, and (d) 5 and 7 days before the flooding. Positive values (warm color) indicate net gain, negative values (cold color) indicate net loss.

adiabatic process when going over the mountains that implies that, unless precipitation happens, the total amount of water, including water droplets and water vapor within the parcel, is conserved.

Tracing back 5–7 days before the flooding (Fig. 15d), there was a small amount of moisture uptake over the Great Lakes region. The water vapor was transported westward and entered the flooding region from the north 5–7 days later. Liu et al. (2016) used a different Lagrangian particle model, the Flexible Particle Dispersion Model (FLEXPART), to estimate moisture sources for this event and obtained similar results. Although the trajectories show that some air parcels originated over the Gulf of Mexico (Fig. 14), the detailed calculations show that most of the uptake from the Gulf precipitated out by the time the parcels reached Kansas and Colorado. However, this does not mean that moisture from the Gulf of Mexico is irrelevant for this case, since it was the initial moisture input to the U.S. Great Plains, so the moisture input from the Gulf of Mexico was mainly indirect. It was previously deposited on the ground through precipitation and then later evaporated to the atmosphere in the U.S. Great Plains.

In general, for the June 2013 Alberta flooding event, considering the moisture uptake between 6 h and 7 days before the flooding, only a small fraction of precipitation originated from the subtropical oceanic regions (e.g., the eastern Pacific) directly, and there was no detectable direct contribution from the Gulf of Mexico or Atlantic Ocean (Fig. 16a). Instead, surface evaporation and evapotranspiration over several regions of the continent represented the dominant source of moisture for this event. In terms of regional contributions (Fig. 16b), 31% was from the U.S. Great Plains, 27% from the western United States, 17% from the Canadian Prairies, 20% from the rest of Canada outside the Prairies, and 5% from the northeastern Pacific. These results suggest that local evaporation and evapotranspiration within the flooding region contributed a small portion of the moisture for the extreme rainfall event, whereas moisture originating from elsewhere on the continent was the key contributor. As such, the conditions of surface water availability (e.g., droughts) or agricultural activities over the U.S. Great Plains could exert indirect but potentially significant effects on the development of flood-producing rainfall events over southern Alberta. Future land-use changes over the U.S. Great Plains together with climate

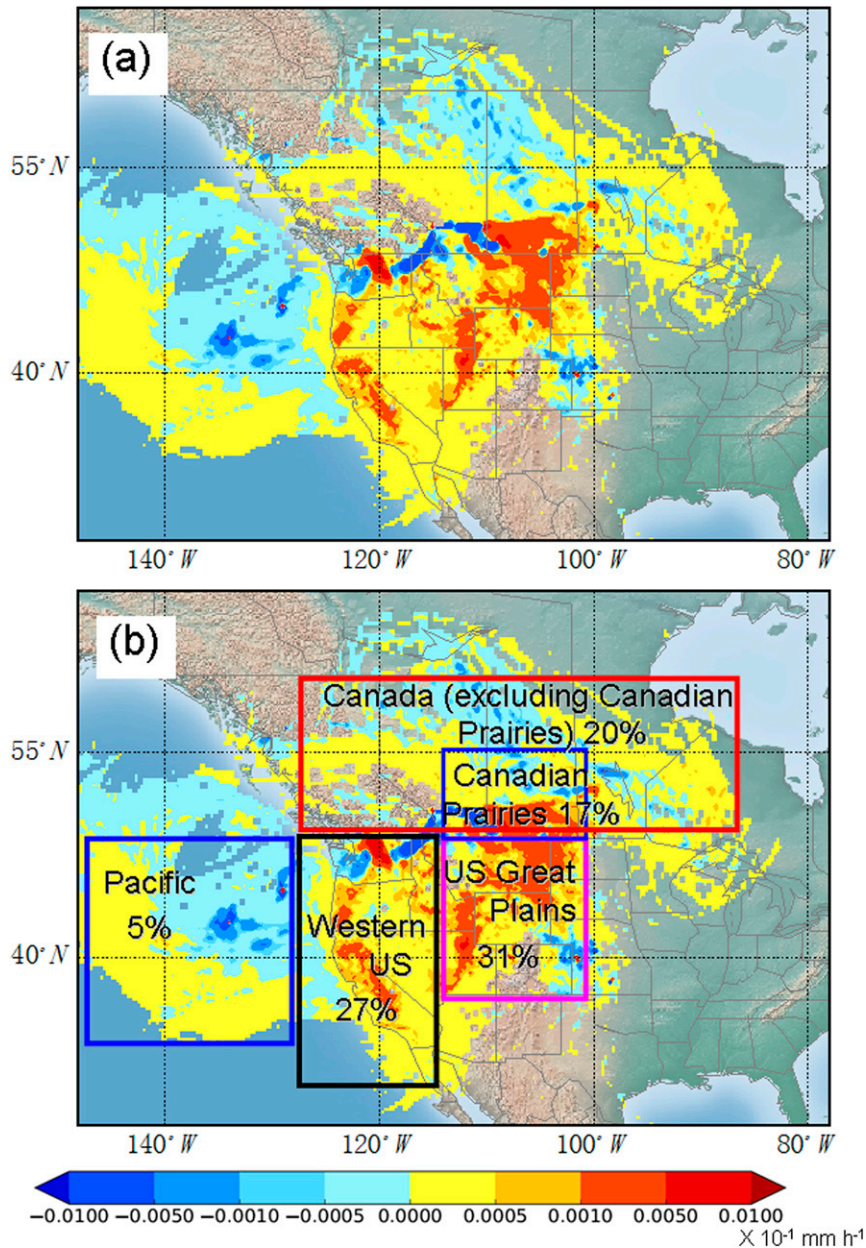


FIG. 16. Moisture uptake (a) between 6 h and 7 days before the flooding. Positive values (warm color) indicate net gain, negative values (cold color) indicate net loss. (b) Contribution (%) of moisture uptake from different regions (highlighted in boxes) for the J13 event.

change could potentially influence these extreme events over the Canadian Prairies.

5. Discussion and conclusions

A devastating and costly flood occurred over southern Alberta during June 2013, which was caused by highly localized and intense rainfall over the foothills and eastern slopes of the Canadian Rockies. The rainfall structure

and its evolution were mainly determined by synoptic-scale flow features that created dynamic forcing and facilitated effective moisture transport into southern Alberta before and during the event. In particular, an enhanced easterly low-level jet located between a cyclonic–anticyclonic dipole transported abundant moisture into southern Alberta and resulted in heavy precipitation. Many characteristics of this system were also typical of previous extreme events that have

occurred in the region (Liu et al. 2016; Szeto et al. 2011). Studies of this event (Pomeroy et al. 2015) and other heavy rainstorms (Moore and Holdsworth 2007; Kumar et al. 2014) suggest that antecedent rainfall moistening the soil during late spring and early summer, especially within a few days before the flooding, leaves the normally arid mountainsides unable to rapidly absorb the additional intense rainfall that results in widespread surface runoff.

High-resolution WRF Model simulations show that the model was able to reproduce both the evolution and structure of the J13 storm precipitation features using a double-moment microphysics scheme. The convection-allowing mesoscale model demonstrated reasonable skill in simulating the evolution of the precipitation patterns, as well as rain rates before and during the flooding. Model diagnostics show that the heavy rainfall resulted from a combination of strong westward moisture advection, the breadth of the axis of significant moisture transport into the flood region, and deep moistening with a nearly saturated PBL. Orographic lifting was the most important forcing initiating convective precipitation along the foothills. Lower-tropospheric frontogenesis and midtropospheric cyclonic vorticity advection became more important for a widespread stratiform precipitation farther away from the foothills during the later stages of the event (Milrad et al. 2015; Liu et al. 2016).

Results from regional water budget assessments suggest that local evaporation and evapotranspiration played a relatively minor role in contributing to the precipitation compared to large-scale moisture transport. Although land surface processes within the precipitation region likely played a secondary role, results from moisture source diagnostics performed by using air parcel back-trajectory techniques suggest that land surface processes over the Great Plains and the Canadian Prairies were instrumental in providing the moisture for the precipitation. Overall, the recycling of evaporated water from the U.S. Great Plains and Midwest was the primary source of moisture for precipitation development for this event. It is also of interest to note that uptake from the Gulf of Mexico typically rained out over the U.S. Great Plains before the air parcels reached the Canadian Prairies.

The fact that the WRF Model was able to replicate many of the observed features of the J13 storm suggests that the model is suitable for numerical studies of similar events. The WRF microphysics scheme sensitivity test for this event suggests that a double-moment scheme may be more suitable for the simulation of the severe events in Alberta. The examination of the convective/stratiform separation algorithm using WRF-simulated radar reflectivity makes it possible to examine how

different types of storm characteristics evolved during the life cycle of the event. The tracing of the remote moisture sources using a back-trajectory analysis method shows that a significant amount of precipitable water actually originated from the south, especially the central Great Plains, and was transported into Alberta through a low-level jet. The results also suggest that the model is suitable for applications in high-resolution regional climate model studies to explore the potential changes in the occurrence frequency and intensity of these extreme orographic rainstorms under a global warming background. Potential changes in storm tracks and surface processes over the continent under climate change could alter the convective regime (Shi and Durran 2015) and the geographical distribution of precipitation over the Prairies. High-resolution regional climate simulations utilizing the WRF Model to explore such changes and their impacts on future extreme rainstorms similar to the J13 event are underway and will be reported elsewhere.

Acknowledgments. We gratefully acknowledge the Natural Sciences and Engineering Research Council of Canada (NSERC) for funding the Changing Cold Regions Network (CCRN) through their Climate Change and Atmospheric Research (CCAR) Initiative. This research is also supported by Environment and Climate Change Canada (ECCC). Y. Li gratefully acknowledges the support from the Global Institute of Water Security at the University of Saskatchewan. L. Chen acknowledge the support from the National Key Research and Development Program with Grant 2016YFA0600403. The authors acknowledge the NOAA Air Resources Laboratory (ARL) for the provision of the HYSPLIT transport and dispersion model and the Real-time Environmental Applications and Display System (READY) website (<http://www.ready.noaa.gov>) used in this publication.

REFERENCES

- Brill, K. F., and F. Mesinger, 2009: Applying a general analytic method for assessing bias sensitivity to bias-adjusted threat and equitable threat scores. *Wea. Forecasting*, **24**, 1748–1754, doi:10.1175/2009WAF2222272.1.
- Brimelow, J., and G. W. Reuter, 2005: Transport of atmospheric moisture during three extreme rainfall events over the Mackenzie River basin. *J. Hydrometeorol.*, **6**, 423–440, doi:10.1175/JHM430.1.
- Bryan, G. H., and H. Morrison, 2012: Sensitivity of a simulated squall line to horizontal resolution and parameterization of microphysics. *Mon. Wea. Rev.*, **140**, 202–225, doi:10.1175/MWR-D-11-00046.1.
- Caracena, F., R. A. Maddox, L. R. Hoxit, and C. F. Chappell, 1979: Mesoanalysis of the Big Thompson storm. *Mon. Wea. Rev.*, **107**, 1–17, doi:10.1175/1520-0493(1979)107<0001:MOTBTS>2.0.CO;2.

- Colle, B., R. Smith, and D. Wesley, 2013: Theory, observations, and predictions of orographic precipitation. *Mountain Weather Research and Forecasting*, F. K. Chow, S. F. J. De Wekker, and B. J. Snyder, Eds., Springer, 291–344, doi:10.1007/978-94-007-4098-3_6.
- Doswell, C. A., III, H. Brooks, and R. Maddox, 1996: Flash forecasting: An ingredient-based methodology. *Wea. Forecasting*, **11**, 560–581, doi:10.1175/1520-0434(1996)011<0560:FFFAIB>2.0.CO;2.
- Durran, D., and J. B. Klemp, 1982: On the effects of moisture on the Brunt–Väisälä frequency. *J. Atmos. Sci.*, **39**, 2152–2158, doi:10.1175/1520-0469(1982)039<2152:OTEOMO>2.0.CO;2.
- Ek, M., and L. Mahrt, 1991: OSU 1-D PBL model user's guide, version 1.04. Dept. of Atmospheric Sciences, Oregon State University, 118 pp. [Available online at <http://ftp.emc.ncep.noaa.gov/mmb/gcp/ldas/nceplsm/OSU1DPBL/OSU1DPBL-userguide.pdf>.]
- Flesch, T. K., and G. W. R. Reuter, 2012: WRF Model simulation of two Alberta flooding events and the impact of topography. *J. Hydrometeor.*, **13**, 695–708, doi:10.1175/JHM-D-11-035.1.
- Garreaud, R., and H. A. Fuenzalida, 2007: The influence of the Andes on cutoff lows: A modeling study. *Mon. Wea. Rev.*, **135**, 1596–1613, doi:10.1175/MWR3350.1.
- Gochis, D., and Coauthors, 2015: The great Colorado flood of September 2013. *Bull. Amer. Meteor. Soc.*, **96**, 1461–1487, doi:10.1175/BAMS-D-13-00241.1.
- Hong, S.-Y., and J.-O. J. Lim, 2006: The WRF single-moment 6-class microphysics scheme (WSM6). *J. Korean Meteor. Soc.*, **42**, 129–151.
- IPCC, 2012: *Managing the Risks of Extreme Events and Disasters to Advance Climate Change Adaptation*. Cambridge University Press, 582 pp.
- Joe, P., and S. Lapczak, 2002: Evolution of the Canadian operational radar network. *Proceedings of ERAD (2002)*, Copernicus, 370–382. [Available online at <http://www.copernicus.org/erad/online/erad-370.pdf>.]
- Kirshbaum, D. J., and D. R. Durran, 2004: Factors governing cellular convection in orographic precipitation. *J. Atmos. Sci.*, **61**, 682–698, doi:10.1175/1520-0469(2004)061<0682:FGCCIO>2.0.CO;2.
- Kochtubajda, B., and Coauthors, 2016: The June 2013 Alberta catastrophic flooding event—Part 2: Fine-scale precipitation and associated features. *Hydrol. Processes*, **30**, 4917–4933, doi:10.1002/hyp.10855.
- Kumar, A., R. A. Houze Jr., K. L. Rasmussen, and C. Peters-Lidard, 2014: Simulation of a flash flooding storm at the steep edge of the Himalayas. *J. Hydrometeor.*, **15**, 212–228, doi:10.1175/JHM-D-12-0155.1.
- LeMone, M. A., M. Tewari, F. Chen, J. Alfieri, and D. Niyogi, 2008: Evaluation of the Noah land-surface model using data from a fair-weather IHOP_200 day with heterogeneous surface fluxes. *Mon. Wea. Rev.*, **136**, 4915–4941, doi:10.1175/2008MWR2354.1.
- Li, Y., and R. B. Smith, 2010: The detection and significance of diurnal pressure and potential vorticity anomalies east of the Rockies. *J. Atmos. Sci.*, **67**, 2734–2751, doi:10.1175/2010JAS3423.1.
- Lim, K.-S. S., and S.-Y. Hong, 2010: Development of an effective double-moment cloud microphysics scheme with prognostic cloud condensation nuclei (CCN) for weather and climate models. *Mon. Wea. Rev.*, **138**, 1587–1612, doi:10.1175/2009MWR2968.1.
- Lin, Y.-L., S. Chiao, T.-A. Wang, and M. L. Kaplan, 2001: Some common ingredients for heavy orographic rainfall. *Wea. Forecasting*, **16**, 633–660, doi:10.1175/1520-0434(2001)016<0633:SCIFHO>2.0.CO;2.
- Liu, A., and Coauthors, 2016: The June 2013 Alberta catastrophic flooding event: Part 1—Climatological aspects and hydrometeorological features. *Hydrol. Processes*, **30**, 4899–4916, doi:10.1002/hyp.10906.
- Maddox, R. A., L. R. Hoxit, C. F. Chappell, and F. Caracena, 1978: Comparison of meteorological aspects of the Big Thompson and Rapid City flash floods. *Mon. Wea. Rev.*, **106**, 375–389, doi:10.1175/1520-0493(1978)106<0375:COMAOT>2.0.CO;2.
- , F. Canova, and L. R. Hoxit, 1980: Meteorological characteristics of flash flood events over the western United States. *Mon. Wea. Rev.*, **108**, 1866–1877, doi:10.1175/1520-0493(1980)108<1866:MCOFFE>2.0.CO;2.
- Mahfouf, J. F., B. Brasnett, and S. Gagnon, 2007: A Canadian Precipitation Analysis (CaPA) project: Description and preliminary results. *Atmos.–Ocean*, **45**, 1–17, doi:10.3137/ao.v450101.
- McDonald, M., and R. Dyck, 2006: 2006 prairie summer severe weather event climatology and verification results report. Meteorological Service of Canada Internal Rep., 31 pp.
- Milrad, S. M., J. R. Gyakum, and E. H. Atallah, 2015: A meteorological analysis of the 2013 Alberta flood: Antecedent large-scale flow pattern and synoptic–dynamic characteristics. *Mon. Wea. Rev.*, **143**, 2817–2841, doi:10.1175/MWR-D-14-00236.1.
- Moore, G. W. K., and G. Holdsworth, 2007: The 25–27 May 2005 Mount Logan storm. Part I: Observations and synoptic overview. *J. Hydrometeor.*, **8**, 590–606, doi:10.1175/JHM586.1.
- Morrison, H., G. Thompson, and V. Tatarskii, 2009: Impact of cloud microphysics on the development of trailing stratiform precipitation in a simulated squall line: Comparison of one- and two-moment schemes. *Mon. Wea. Rev.*, **137**, 991–1007, doi:10.1175/2008MWR2556.1.
- Neiman, P. J., F. M. Ralph, G. A. Wick, J. D. Lundquist, and M. D. Dettinger, 2008: Meteorological characteristics and overland precipitation impacts of atmospheric rivers affecting the west coast of North America based on eight years of SSM/I satellite observations. *J. Hydrometeor.*, **9**, 22–47, doi:10.1175/2007JHM855.1.
- NOAA/NWS/NCEP, 2000: NCEP FNL operational model global tropospheric analyses, continuing from July 1999, updated daily. Research Data Archive at the National Center for Atmospheric Research, Computational and Information Systems Laboratory, accessed 1 July 2014, doi:10.5065/D6M043C6.
- Oleson, K. W., and Coauthors, 2004: Technical description of the Community Land Model (CLM). NCAR Tech. Note NCAR/TN-461+STR, 173 pp., doi:10.5065/D6N877R0.
- Pennelly, C., G. Reuter, and T. Flesch, 2014: Verification of the WRF Model for simulating heavy precipitation in Alberta. *Atmos. Res.*, **135–136**, 172–192, doi:10.1016/j.atmosres.2013.09.004.
- Pomeroy, J., R. E. Stewart, and P. H. Whitfield, 2015: The 2013 flood event in the South Saskatchewan and Elk River basins: Causes, assessment and damages. *Can. Water Resour. J.*, **41**, 105–117, doi:10.1080/07011784.2015.1089190.
- Raddatz, R. L., 2000: Summer rainfall recycling for an agricultural region of the Canadian prairies. *Can. J. Soil Sci.*, **80**, 367–373, doi:10.4141/S99-016.
- Rasmussen, K. L., and R. A. Houze Jr., 2012: Flash flooding at the steep edge of high terrain: Disaster in the Himalayas.

- Bull. Amer. Meteor. Soc.*, **93**, 1713–1724, doi:10.1175/BAMS-D-11-00236.1.
- , A. J. Hill, V. E. Toma, M. D. Zuluaga, P. J. Webster, and R. A. Houze, 2015: Multiscale analysis of three consecutive years of anomalous flooding in Pakistan. *Quart. J. Roy. Meteor. Soc.*, **141**, 1259–1276, doi:10.1002/qj.2433.
- Schumacher, R. S., and R. H. Johnson, 2005: Organization and environmental properties of extreme-rain-producing mesoscale convective systems. *Mon. Wea. Rev.*, **133**, 961–976, doi:10.1175/MWR2899.1.
- Seneviratne, S. I., T. Corti, E. L. Davin, M. Hirschi, E. B. Jaeger, I. Lehner, B. Orlowsky, and A. J. Teuling, 2010: Investigating soil moisture–climate interactions in a changing climate: A review. *Earth Sci. Rev.*, **99**, 125–161, doi:10.1016/j.earscirev.2010.02.004.
- Shi, X., and D. R. Durran, 2015: Estimating the response of extreme precipitation over midlatitude mountains to global warming. *J. Climate*, **28**, 4246–4262, doi:10.1175/JCLI-D-14-00750.1.
- Shook, K., and J. Pomeroy, 2012: Changes in the hydrological character of rainfall on the Canadian prairies. *Hydrol. Processes*, **26**, 1752–1766, doi:10.1002/hyp.9383.
- Skamarock, W. C., and Coauthors, 2008: A description of the Advanced Research WRF version 3. NCAR Tech. Note NCAR/TN-475+STR, 113 pp., doi:10.5065/D68S4MVH.
- Smirnova, T. G., J. M. Brown, and S. G. Benjamin, 1997: Performance of different soil model configurations in simulating ground surface temperature and surface fluxes. *Mon. Wea. Rev.*, **125**, 1870–1884, doi:10.1175/1520-0493(1997)125<1870:PODSMC>2.0.CO;2.
- , —, —, and D. Kim, 2000: Parameterization of cold-season processes in the MAPS land-surface scheme. *J. Geophys. Res.*, **105**, 4077–4086, doi:10.1029/1999JD901047.
- Smith, J. A., M. L. Baeck, G. Villarini, D. B. Wright, and W. Krajewski, 2013: Extreme flood response: The June 2008 flooding in Iowa. *J. Hydrometeorol.*, **14**, 1810–1825, doi:10.1175/JHM-D-12-0191.1.
- Sodemann, H., C. Schwierz, and H. Wernli, 2008: Interannual variability of Greenland winter precipitation sources: Lagrangian moisture diagnostic and North Atlantic Oscillation influence. *J. Geophys. Res.*, **113**, D12111, doi:10.1029/2007JD009416.
- Stein, A. F., R. R. Draxler, G. D. Rolph, B. J. B. Stunder, M. D. Cohen, and F. Ngan, 2015: NOAA's HYSPLIT atmospheric transport and dispersion modeling system. *Bull. Amer. Meteor. Soc.*, **96**, 2059–2077, doi:10.1175/BAMS-D-14-00110.1.
- Steiner, M., R. A. Houze Jr., and S. E. Yuter, 1995: Climatological characterization of three-dimensional storm structure from radar and rain gauge data. *J. Appl. Meteor.*, **34**, 1978–2007, doi:10.1175/1520-0450(1995)034<1978:CCOTDS>2.0.CO;2.
- Stohl, A., and P. James, 2004: A Lagrangian analysis of the atmospheric branch of the global water cycle. Part I: Method description, validation, and demonstration for the August 2002 flooding in central Europe. *J. Hydrometeorol.*, **5**, 656–678, doi:10.1175/1525-7541(2004)005<0656:ALAOTA>2.0.CO;2.
- Szeto, K., W. Henson, R. E. Stewart, and G. Gascon, 2011: The catastrophic June 2002 rainstorm. *Atmos.–Ocean*, **49**, 380–395, doi:10.1080/07055900.2011.623079.
- , P. Gysbers, J. Brimelow, and R. Stewart, 2015: The 2014 extreme flood on the southeastern Canadian Prairies. *Bull. Amer. Meteor. Soc.*, **96**, S20–S24, doi:10.1175/BAMS-D-15-00110.1.
- Thompson, G., P. R. Field, R. M. Rasmussen, and W. D. Hall, 2008: Explicit forecasts of winter precipitation using an improved bulk microphysics scheme. Part II: Implementation of a new snow parameterization. *Mon. Wea. Rev.*, **136**, 5095–5115, doi:10.1175/2008MWR2387.1.
- Turato, B., O. Reale, and F. Siccardi, 2004: Water vapor sources of the October 2000 Piedmont flood. *J. Hydrometeorol.*, **5**, 693–712, doi:10.1175/1525-7541(2004)005<0693:WVSOTO>2.0.CO;2.
- Viterbo, F., J. Hardenberg, A. Provenzale, L. Molini, A. Parodi, O. O. Sy, and S. Tanelli, 2016: High-resolution simulations of the 2010 Pakistan flood event: Sensitivity to parameterizations and initialization time. *J. Hydrometeorol.*, **17**, 1147–1167, doi:10.1175/JHM-D-15-0098.1.
- Wheater, H. S., and P. Gober, 2013: Water security in the Canadian prairies: Science and management challenges. *Philos. Trans. Roy. Soc. London*, **371A**, 20120409, doi:10.1098/rsta.2012.0409.
- Zhang, X., L. A. Vincent, W. D. Hogg, and A. Niitsoo, 2000: Temperature and precipitation trends in Canada during the 20th century. *Atmos.–Ocean*, **38**, 395–429, doi:10.1080/07055900.2000.9649654.
- , W. D. Hogg, and E. Mekis, 2001: Spatial and temporal characteristics of heavy precipitation events over Canada. *J. Climate*, **14**, 1923–1936, doi:10.1175/1520-0442(2001)014<1923:SATCOH>2.0.CO;2.